AMERICAN SOCIETY FOR MICROBIOLOGY | Journal of Virology

Host-Microbial Interactions | Full-Length Text

Enterovirus 3A protein disrupts endoplasmic reticulum homeostasis through interaction with GBF1

Junki Hirano,[1,2,3] Tsuyoshi Hayashi,[3] Kouichi Kitamura,[3] Yorihiro Nishimura,[3] Hiroyuki Shimizu,[3] Toru Okamoto,[4,5] Kazuma Okada,[1,2] Kentaro Uemura,[1,2] Ming Te Yeh,[2,6] Chikako Ono,[1,2] Shuhei Taguwa,[1,2,6] Masamichi Muramatsu,[3,7] Yoshiharu Matsuura[1,2,6]

AUTHOR AFFILIATIONS See affiliation list on p. 25.

ABSTRACT Enteroviruses are single-stranded, positive-sense RNA viruses causing endoplasmic reticulum (ER) stress to induce or modulate downstream signaling pathways known as the unfolded protein responses (UPR). However, viral and host factors involved in the UPR related to viral pathogenesis remain unclear. In the present study, we aimed to identify the major regulator of enterovirus-induced UPR and elucidate the underlying molecular mechanisms. We showed that host Golgi-specific brefeldin A-resistant guanine nucleotide exchange factor 1 (GBF1), which supports enteroviruses replication, was a major regulator of the UPR caused by infection with enteroviruses. In addition, we found that severe UPR was induced by the expression of 3A proteins encoded in human pathogenic enteroviruses, such as enterovirus A71, coxsackievirus B3, poliovirus, and enterovirus D68. The N-terminal-conserved residues of 3A protein interact with the GBF1 and induce UPR through inhibition of ADP-ribosylation factor 1 (ARF1) activation via GBF1 sequestration. Remodeling and expansion of ER and accumulation of ER-resident proteins were observed in cells infected with enteroviruses. Finally, 3A induced apoptosis in cells infected with enteroviruses via activation of the protein kinase RNA-like endoplasmic reticulum kinase (PERK)/C/EBP homologous protein (CHOP) pathway of UPR. Pharmaceutical inhibition of PERK suppressed the cell death caused by infection with enteroviruses, suggesting the UPR pathway is a therapeutic target for treating diseases caused by infection with enteroviruses.

IMPORTANCE Infection caused by several plus-stranded RNA viruses leads to dysregulated ER homeostasis in the host cells. The mechanisms underlying the disruption and impairment of ER homeostasis and its significance in pathogenesis upon enteroviral infection remain unclear. Our findings suggested that the 3A protein encoded in human pathogenic enteroviruses disrupts ER homeostasis by interacting with GBF1, a major regulator of UPR. Enterovirus-mediated infections drive ER into pathogenic conditions, where ER-resident proteins are accumulated. Furthermore, in such scenarios, the PERK/CHOP signaling pathway induced by an unresolved imbalance of ER homeostasis essentially drives apoptosis. Therefore, elucidating the mechanisms underlying the virus-induced disruption of ER homeostasis might be a potential target to mitigate the pathogenesis of enteroviruses.

KEYWORDS enterovirus, GBF1, ER stress, unfolded protein response, PERK, apoptosis

The endoplasmic reticulum (ER) comprises an extensive network of membranes responsible for multiple roles in the cell, including protein production, lipid synthesis, and calcium storage (1). Disruption of ER homeostasis, called ER stress, activates the unfolded protein responses (UPR). Mild and transient ER stress activates UPR to restore ER homeostasis, whereas severe and prolonged ER stress triggers the protein kinase RNA-like endoplasmic reticulum kinase (PERK)/C/EBP homologous

Editor Christiane E. Wobus, University of Michigan Medical School, Ann Arbor, Michigan, USA

Address correspondence to Yoshiharu Matsuura, matsuura@biken.osaka-u.ac.jp.

The authors declare no conflict of interest.

See the funding table on p. 26.

Received 9 May 2024
Accepted 10 May 2024
Published 21 June 2024

protein (CHOP) pathway of UPR, resulting in apoptosis (2). UPR is associated with various disorders, such as neurodegenerative diseases, cancers, metabolic diseases, and infectious diseases (3, 4). Therefore, appropriate levels of UPR must be maintained to decrease the risk of undesired health complications.

RNA viruses significantly remodel the cellular endomembrane system, affecting functions of subcellular organelles, including the ER. Many positive-stranded RNA viruses reportedly induce or modulate UPR. However, the impact of virus-associated UPR on virus replication and pathogenesis needs to be better understood (5). Therefore, the molecular mechanisms underlying viral infection-induced UPR must be investigated to characterize and mitigate their pathogenesis.

The genus *Enterovirus* (family *Picornaviridae*) comprises a highly diverse group of viruses harboring a single-stranded positive RNA genome, including poliovirus (PV) and non-polio viruses, such as enterovirus A71 (EV-A71), D68 (EV-D68), and coxsackievirus B3 (CVB3). Multiple disorders, including hand-foot-and-mouth disease, poliomyelitis, herpangina, and the common cold, are caused by enteroviruses (6). Furthermore, enterovirus-induced meningitis, encephalopathy, encephalitis, acute flaccid paralysis, and myocarditis pose a threat to child healthcare worldwide; however, the underlying pathogenic mechanisms remain unclear. Although potent vaccines nearly eradicated the poliovirus, effective vaccines or therapeutic strategies against non-polio enteroviruses remain lacking. Therefore, investigating viral and host factors involved in viral pathogenesis is warranted to control enterovirus-induced diseases.

EV-A71 has caused severe outbreaks of hand-foot-and-mouth disease in the Asia-Pacific region since the end of the 1990s (7). Genomic RNA of EV-A71 is translated into a single polyprotein that is proteolytically processed into four structural (VP1, VP2, VP3, and VP4) and seven non-structural (2A, 2B, 2C, 3A, 3B, 3C, and 3D) proteins. Structural proteins form the viral capsid, whereas the non-structural proteins are localized in the viral replication organelle (RO), recruiting host proteins to support the replication of the viral RNA (8). The 3A protein of enterovirus, localized in the RO, is a multifunctional protein that, together with the viral 2BC protein, participates in the formation of RO (9). Furthermore, the 3A protein inhibits protein trafficking and interacts with multiple host proteins, such as Golgi-specific brefeldin A-resistant guanine nucleotide exchange factor 1 (GBF1), acyl-CoA binding domain containing 3 (ACBD3), serine protease 3, and secretory carrier membrane protein 3, to support virus replication (10–16). However, the mechanisms by which 3A regulates host function still need to be better characterized.

Among the positive-stranded RNA viruses, flaviviruses and coronaviruses mainly modulate ER membranes for replication (17–20). These viruses disrupt ER homeostasis through their encoded proteins (21–23); however, the relationship between ER homeostasis and enterovirus infection is not fully understood. The RO of enteroviruses is derived from both ER and Golgi membranes (24), which come in contact with ER through oxysterol-binding protein 1 (OSBP), thus transferring the lipids necessary for viral replication (25). BiP, an ER-localized chaperone protein and UPR marker, circumvents the enterovirus-mediated inactivation of the host mRNA translation (26). BiP mRNA contains an internal ribosome entry site (IRES), and its expression is enhanced during poliovirus infection (26, 27). Furthermore, EV-A71 and CVB3 induce or modulate UPR by as yet unknown mechanisms (28–30). Therefore, the molecular mechanisms and biological significance of UPR during enterovirus infection warrant further investigation. In the present study, we aimed to identify the major regulator of enterovirus-induced UPR and elucidate the underlying molecular mechanisms.

RESULTS

EV-A71 infection induces the UPR through viral 3A protein

Consistent with previous reports showing that the UPR pathways are induced or modulated during EV-A71 infection (28, 29), we observed that the mRNA level of some UPR markers, including *BiP*, *XBP1s*, and *CHOP*, was significantly increased with EV-A71 infection in a dose-dependent manner (Fig. 1A). Accordingly, the protein level of BiP,

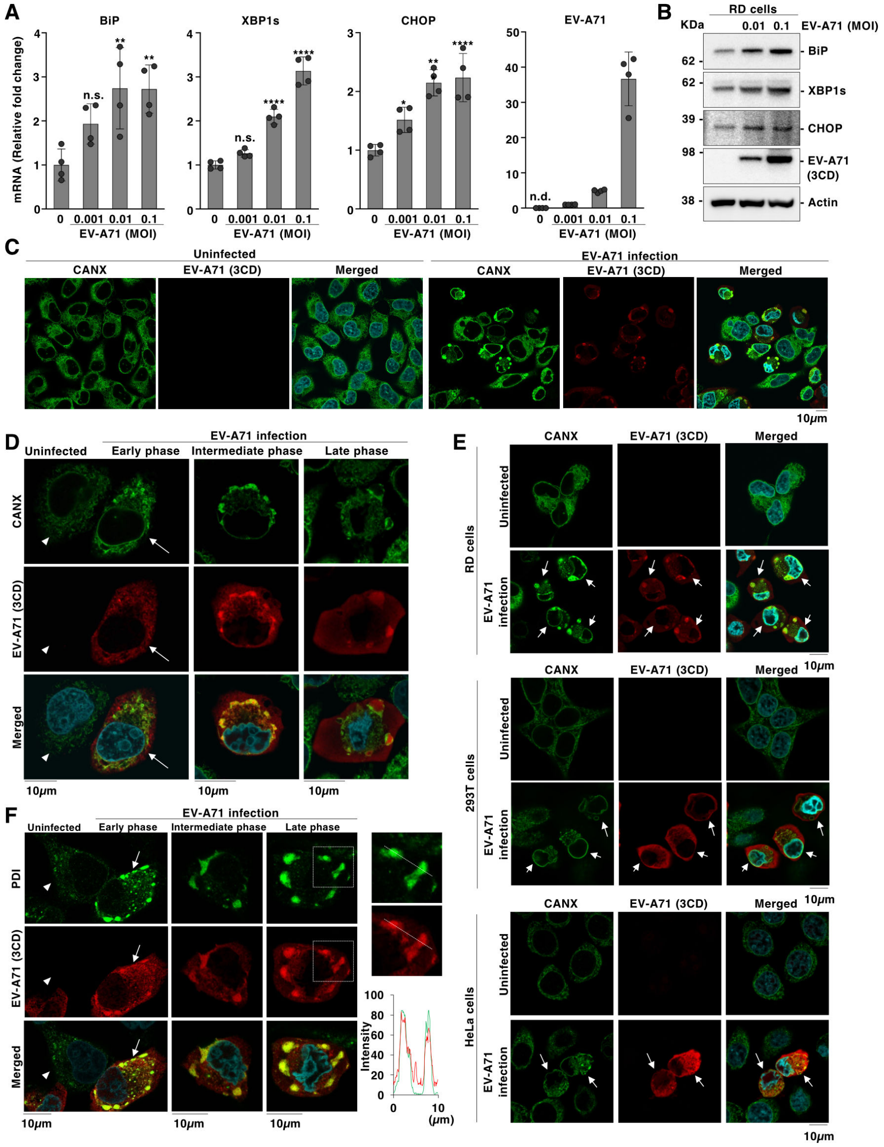

FIG 1 EV-A71 infection alters ER homeostasis and morphology. (A) Expression of BiP, XBP1s, CHOP, and viral RNA in RD cells infected with EV-A71 at an MOI of 0.001, 0.01, and 0.1 was quantified using qPCR at 36 h post-infection. (B) Expression levels of BiP, XBP1s, CHOP, and EV-A71 3CD protein in RD cells infected with EV-A71 at an MOI of 0.01 and 0.1 were detected using immunoblotting at 36 h post-infection. (C) RD cells infected with EV-A71 at an MOI of 0.3 were incubated for 30 h and stained with anti-CANX antibody, anti-EV-A71 3CD antibody, and DAPI; fluorescent signals were detected using microscopy (FV-3000, OLYMPUS). The scale bar represents 10 µm. (D) RD cells infected with EV-A71 at an MOI of 0.3 were incubated for 8 h (early phase), 16 h (intermediate phase), or 30 h (late phase) and stained with anti-CANX antibody, anti-EV-A71 3CD antibody, and DAPI. The fluorescent signals were detected using microscopy. The arrowhead and straight arrow represent uninfected and EV-A71-infected cells, respectively. The scale bars represent 10 µm. (E) RD, HEK293T, and HeLa cells infected with EV-A71 at an MOI of 0.3 were incubated for 30 h and stained with anti-CANX antibody, anti-EV-A71 3CD antibody, and DAPI; fluorescent signals were detected using microscopy. Arrows indicate EV-A71-infected cells. The scale bar represents 10 µm. (F) RD cells infected with EV-A71 at an MOI of 0.3 were incubated for 8 h (early phase), 16 h (intermediate phase), or 30 h (late phase) and stained with anti-PDI antibody, anti-EV-A71 3CD antibody, and DAPI. The fluorescent signals were detected using microscopy. The arrowhead and straight arrow represent uninfected and EV-A71-infected cells, respectively. The scale bars represent 10 µm (*Left*). The colocalization analysis was performed using Fiji software (*Right*). The data presented in A denote mean ±

(Continued on next page)

FIG 1 (Continued)

S.D. of two independent experiments; those in B-F are representative of two independent experiments. For the experiment presented in A significance (*$P \leq 0.05$; **$P \leq 0.01$; ****$P \leq 0.00001$; n.s., not significant; n.d., not detected) was determined using one-way analysis of variance (ANOVA) test ($n = 4$).

XBP1s, and CHOP in EV-A71 infected cells also increased after EV-A71 infection (Fig. 1B). To confirm the effect of EV-A71 infection on the ER remodeling, the localization of some ER markers was examined using immune-fluorescent staining. We found that calnexin (CANX, an ER membrane marker) was distributed in the cytoplasm in uninfected cells but concentrated at the juxtanuclear area in response to EV-A71 infection (Fig. 1C and D). Similar changes in the accumulation of CANX and ER morphology were observed in EV-A71-infected HEK293T and HeLa cells (Fig. 1E). In addition, our immune-fluorescent analysis showed that protein disulfide isomerase (PDI, a marker of ER lumen) was expressed as discrete puncta at a low level in the cytoplasm of uninfected cells. In contrast, the PDI showed accumulated structures in the infected cells, and the PDI signals merged with the viral 3CD (Fig. 1F). These data indicate that EV-A71 infection alters ER morphology.

As the localization of ER marker proteins drastically remodeled during EV-A71 infection, we examined the localization of the RO and the modified ER structure. Viral proteins 2B, 2C, and 3AB localized in the RO did not merge with the CANX during EV-A71 infection (Fig. 2A). Furthermore, 3D reconstitution analysis on EV-A71-infected RD cells showed distinct localization of CANX and the viral 2B protein (Fig. 2B). Collectively, these data indicate that EV-A71 infection alters the ER structure that is distinct from the RO.

To determine how EV-A71 modulates ER homeostasis, we transiently over-expressed viral proteins and their precursors to identify the effector viral protein. Our qPCR analysis showed that the mRNA level of BiP in the 3A over-expressed cells increased approximately 3-fold compared with that in the mock and GFP controls (Fig. 2C). Furthermore, the changes in BiP mRNA and protein levels in the presence of the 3A protein were dose-dependent in RD cells (Fig. 2D and E) and could be reproduced in HEK293 T cells or HT-29 cells (Fig. 2F). Besides BiP, the increased mRNA level in the presence of 3A protein was observed for other UPR-related genes such as *XBP1s, CHOP*, *CANX*, *GRP94*, *PDI*, *EDEM1*, or *HERPD1* (Fig. 2G). Although the expression level of the 3A protein was moderate compared with that of the other viral proteins (Fig. 2H through L), only the presence of the viral 3A protein specifically increased the expression of UPR-related genes, suggesting that EV-A71 modulates ER homeostasis through its 3A protein.

3A protein of EV-A71 activates all branches of the UPR pathways

The UPR can be initiated by the IRE1-, ATF6-, and PERK-mediated pathways. To further characterize how the 3A protein induces UPR, we first assessed IRE1 activation with *XBP1* mRNA splicing as the activation marker using a reporter construct expressing mNeonGreen fused to a nuclear localization signal (NLS) (Fig. 3A *Upper*). The fluorescent signal of mNeonGreen was observed in the nuclei of cells co-expressing the reporter construct with mCherry-tagged 3A but not in those with mCherry alone (Fig. 3A *lower* and 3B). Furthermore, 3A protein expression enhanced the mRNA and protein levels of XBP1s in a dose-dependent manner (Fig. 3C and D).

ATF6 activation leads to its site-1 and site-2 protease-mediated cleavage at the Golgi apparatus and subsequent nuclear localization of the N-terminal ATF6 fragment. To determine whether the 3A protein modulates the UPR through ATF6, the AcGFP-tagged ATF6, and the mCherry-tagged 3A were co-expressed in RD cells to determine the localization of the cleaved ATF6. Nuclear localization of ATF6 was observed only in the presence of the mCherry-tagged 3A (Fig. 3E), along with ATF6 cleavage by the 3A protein, in a dose-dependent manner (Fig. 3F).

To determine whether the 3A protein modulates UPR via the PERK that activates the ATF4/CHOP, a reporter construct expressing amino acids 1–28 of ATF4 fused to mScarlet-I and NLS under the control of IRES in the 5′ non-translated region of ATF4 gene (Fig. 3G

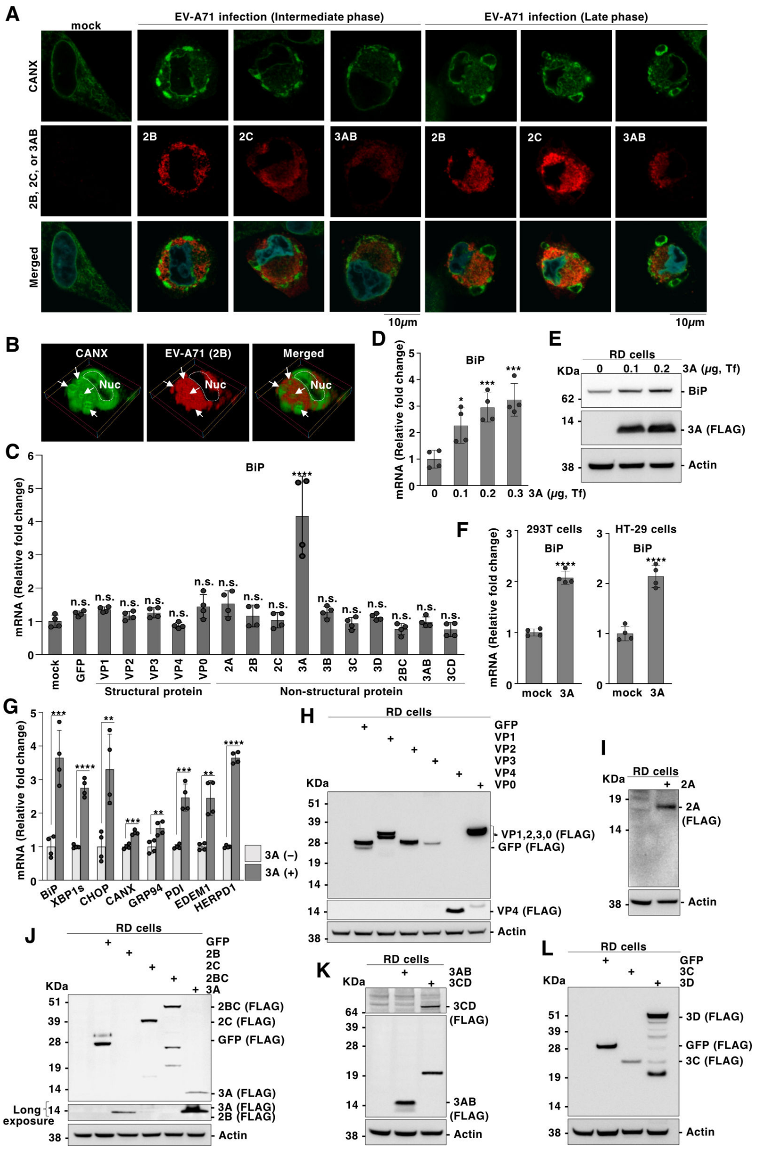

FIG 2 EV-A71 infection alters ER homeostasis through viral 3A protein. (A) RD cells infected with EV-A71 at an MOI of 0.3 were incubated for 16 h (intermediate phase) or 30 h (late phase) and stained with anti-CANX antibody, anti-EV-A71 2B, 2C, or 3AB antibody, and DAPI; fluorescent signals were detected using microscopy. The scale bar represents 10 µm. (B) RD cells infected with EV-A71 at an MOI of 0.3 were incubated for 30 h and stained with anti-CANX and anti-EV-A71 2B antibodies. The fluorescent signals were detected using microscopy, and 3D reconstitution was performed using the cellSens imaging software (OLYMPUS). Nuc, nucleus. The straight arrows indicate the cytoplasmic structure of EV-A71-infected cells. (C) RD cells were transfected with GFP, viral proteins of EV-A71 (VP1, VP2, VP3, VP4, 2A, 2B, 2C, 3A 3B, 3C, or 3D), or its precursors (VP0, 2BC, 3AB, or 3CD). *BiP* expression was quantified using qPCR at 48 h post-transfection. RD cells were transfected with an increasing amount of a plasmid encoding 3A protein, and *BiP* expression was detected using qPCR (D) and immunoblotting (E) at 48 h post-transfection. Tf, transfection. (F) Expression of BiP in HEK293T cells (*Left*) or HT-29 cells (*Right*) expressing 3A was quantified using qPCR at 48 h post-transfection. (G) RD cells were transfected with 3A protein, and expression of genes related to UPR (*BiP*, *XBP1s*, *CHOP*, *CANX*, *GRP94*, *PDI*, *EDEM1*, or *HERPD1*) was quantified using qPCR at 48 h post-transfection. (H-L) Expression of GFP, VP1, VP2, VP3, VP4, VP0, 2A, 2B, 2C, 3A, 3C, 3D, 2BC, 3AB, or 3CD in RD cells was detected using immunoblotting. The transfected amounts of plasmid presented in each figure were calculated based on 24-well plates. The data presented in C, D, F, and G denote mean ± S.D. of two independent experiments; those in A, B, E, and H-L are representative

(Continued on next page)

FIG 2 (Continued)

of two independent experiments. For the experiments presented in C, D, and F, significance (*$P \leq 0.05$; **$P \leq 0.01$; ***$P \leq 0.001$; ****$P \leq 0.00001$; n.s., not significant) was determined using one-way ANOVA test ($n = 4$). For the experiment presented in G, significance (**$P \leq 0.01$; ***$P \leq 0.001$; ****$P \leq 0.00001$) was determined using Student's *t*-test ($n = 4$).

Upper) was co-expressed with AcGFP-tagged 3A in RD cells. Nuclear fluorescence of mScarlet-I was detected in cells co-expressing AcGFP-tagged 3A but not in those expressing AcGFP alone (Fig. 3G *Lower* and 3H). We also observed the increased expression levels of the CHOP mRNA and protein in a dose-dependent manner by the over-expressed 3A protein (Fig. 3I and J).

We then examined whether other EV-A71 non-structural proteins, such as 2B, 2C, and 2BC, induce UPR pathways. In contrast to the expression of the 3A protein, the expression of 2B, 2C, or 2BC did not activate the XBP1s or ATF4 reporter (Fig. 4A and B). Similarly, 2B, 2C, or 2BC did not induce the cleavage of ATF6 (Fig. 4C). Moreover, the expression of these proteins did not induce the BiP, XBP1s, or CHOP mRNAs or proteins (Fig. 4D and E). These data indicate that the expression of 3A of EV-A71 specifically induces severe ER stress and activates all branches of the UPR.

Enterovirus infection induces ER stress-dependent cell death

To further explore the significance of the UPR pathways to EV-A71 during infection, we examined virus phenotypes in cells with each UPR branch suppressed by specific inhibitors (Fig. 5A), which showed little toxicity up to 10 µM in RD cells (Fig. 5B). Among the tested inhibitors, only the PERK inhibitor I (PERKi I) significantly reduced the plaque size of EV-A71 (Fig. 5C through E). The plaque size of EV-A71 was similarly reduced when treated with AMG PERK 44, another selective inhibitor of PERK (Fig. 5F through H). However, virus titers in cells treated with up to 10 µM of these UPR inhibitors were comparable with the DMSO control and significantly suppressed by Rupintrivir, a known inhibitor against EV-A71 (31, 32) (Fig. 5I). In addition, the intracellular viral RNA level was decreased only when treated with a relatively high concentration (10 µM) of the UPR inhibitors (Fig. 5J). Collectively, the PERKi I reduced the plaque size of EV-A71 (Fig. 5C and D) without a significant impact on virus propagation (Fig. 5I and J), implying an effect on cell death that prevented or delayed virus release (Fig. 6A).

To further test this hypothesis, we examined the cleavage of Poly (ADP-ribose) polymerase (PARP) to monitor apoptosis. PARP cleavage in EV-A71-infected RD cells was inhibited by the treatment with >0.1 µM PERKi I (Fig. 6B and C). The activities of caspase-3 and caspase-7, which were induced during EV-A71 infection, were suppressed by treatment with 3 µM of PERKi I (Fig. 6D). Besides virus infection, we also confirmed that 3A protein itself could induce apoptotic activity through the PERK pathway in a dose-dependent manner (Fig. 3G through J, 6E, and F).

We examined whether the same effect of the 3A protein on the UPR is conserved among other human enteroviral pathogens. Enhanced expression of BiP, XBP1s, and CHOP was observed in cells infected with CVB3 (strain Kandolf, Enterovirus B), PV1 (strain Sabin, Enterovirus C), and EV-D68 (strain Fermon, Enterovirus D) (Fig. 6G) or those with over-expressed individual 3A protein (Fig. 6H and I). Moreover, treatment with PERKi I significantly reduced the plaque size of these enteroviruses (Fig. 6J and K). These data indicate that the enteroviruses induce apoptosis via the PERK pathway.

Ile^{8} and Ile^{10} of 3A participate in the UPR via the inhibition of protein transport

Next, we generated a series of 3A mutant constructs (Fig. 7A) to identify the amino acid residues responsible for the UPR induction. Deleting the C-terminal region of 3A impaired its expression in both soluble and pellet fractions of cell lysates owing to proteasomal degradation (Fig. 7B and C). Conversely, protein expression of the 3A was not affected by the various N-terminal deletions (Fig. 7A, D, and E); however, compared

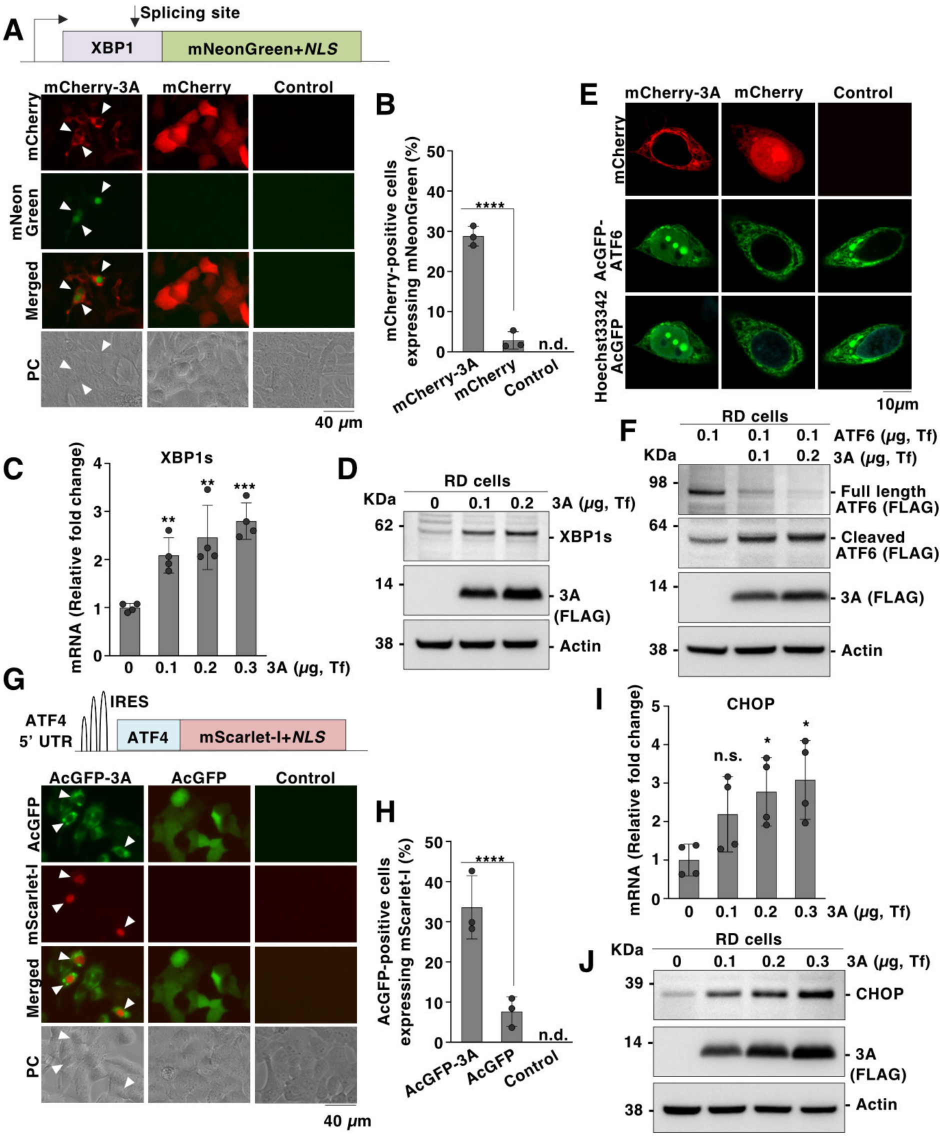

FIG 3 3A protein of EV-A71 activates UPR pathways. (A) The structure of the reporter vector detecting XBP1 splicing (Addgene, #115968) (*Upper*). RD cells transfected with a plasmid encoding N-terminal mCherry-tagged 3A protein and the reporter vector. The fluorescent signals were detected using microscopy at 24 h post-transfection. Arrowhead: mNeonGreen-positive cells. The scale bar represents 40 μm. (B) The row data of fluorescent images obtained from the experiment in Fig. 2A (20× magnification, *n* = 3 in each experiment) were quantified using Fiji software to determine the percentage of mCherry-positive cells expressing mNeonGreen. RD cells were transfected with increasing concentrations of the 3A protein, and XBP1s expression was detected using qPCR (C) and immunoblotting (D) at 48 h post-transfection. RD cells were transfected with N-terminal AcGFP-tagged ATF6 and N-terminal mCherry-tagged 3A protein; (E) fluorescent signals were detected using microscopy at 48 h post-transfection. The scale bar represents 10 μm. (F) Expression levels of full-length ATF6, cleaved ATF6, and 3A protein were detected using immunoblotting at 48 h post-transfection using an anti-FLAG antibody. (G) The structure of the reporter vector detecting induction of ATF4 (Addgene, #115969) (*Upper*). RD cells co-transfected with a plasmid encoding N-terminal AcGFP-tagged 3A protein, and the reporter vector and fluorescent signals were detected using microscopy at 24 h post-transfection. Arrowhead, mScarlet-I-positive cells. The scale bar represents 40 μm. (H) The row data of fluorescent images obtained from the experiment in Fig. 2G (20× magnification, *n* = 3 in each experiment) were quantified using Fiji software to determine the percentage of AcGFP-positive cells expressing mScarlet-I. RD cells were transfected with an increasing amount of a plasmid encoding 3A protein, and CHOP expression was detected using qPCR (I) and immunoblotting (J) at 48 h post-transfection. The transfected amounts of plasmid presented in each figure were calculated based on 24-well plates. The data presented in C and I denote mean ± S.D. of two independent experiments; those

(Continued on next page)

FIG 3 (Continued)

in A, B, D–H, and J are representative of two independent experiments. Significance (*$P \leq 0.05$; **$P \leq 0.01$; ***$P \leq 0.001$; ****$P \leq 0.00001$; n.s., not significant) was determined using one-way ANOVA test ($n = 4$).

with the wild-type 3A, these truncated 3A proteins significantly attenuated the mRNA levels of *BiP* and *XBP1s* (Fig. 7H). Subsequently, we conducted alanine-scanning mutagenesis of 10 N-terminal amino acids of 3A (Fig. 7A, F, and G), which revealed that the substitution of Ile^8 or Ile^{10} in 3A to Ala (3A-I8A or -I10A) significantly reduced the induction of BiP and XBP1s, without affecting the 3A expression (Fig. 7G and I). Although a reduced mRNA level of *BiP* and *XBP1s* was observed in response to the substitution of Arg^6 or Arg ^{9} in 3A to Ala (Fig. 7H), it could be due to the reduced expression of these mutant 3A proteins as indicated by the western blot (Fig. 7G). Therefore, we focused on 3A-Ile^8 and Ile^{10}. In addition, our sequence analysis showed that these Ile residues in the N-terminus of 3A are highly conserved among various enterovirus species (Fig. 7J). Furthermore, structural modeling of the N-terminal region of 3A revealed that the side chains of Ile^8 and Ile^{10} were exposed to the protein surface (Fig. 7K).

To examine the significance of the 3A protein as an inducer of UPR pathways during EV-A71 infection, we generated recombinant EV-A71 strains that carried alanine substitutions of Ile^8 (EV-A71-3A-I8A) or Ile^{10} (EV-A71-3A-I10A). Although EV-A71-3A-I10A exhibited an attenuated viral titer at the time of generation of the virus (Fig. 7L), EV-A71-3A-I8A showed normal growth kinetics (Fig. 7M). Therefore, we examined the ability of EV-A71-3A-I8A to induce BiP or XBP1s mRNA. Upon infection, EV-A71-3A-I8A caused reduced expression of BiP or XBP1s compared with the wild-type virus (Fig. 7N); however, the infectious titer of both viruses was the same (Fig. 7O). These results suggest that the function of the 3A protein is crucial for the activation of UPR pathways during the infection.

Since the N-terminal region of 3A is crucial for interaction with multiple host proteins (10–16), and 3A-I8A and 3A-I10A failed to induce a comparable mRNA level of *BiP* and *XBP1s*, we examined the role of the two amino acid positions in mediating UPR. Our pull-down assay showed that the wild-type 3A (WT), as well as 3A-I8A and 3A-I10A, bound BiP (Fig. 8A). However, 3A-I8A and 3A-I10A failed to increase the *BiP* mRNA level, suggesting that the binding of 3A to BiP may not be directly involved in mediating UPR.

To identify the molecular pathways for the EV-A71 3A to regulate the UPR, we performed RNA sequencing (RNA-seq) with cells expressing either WT or mutant 3A (Fig. 8B). Although the expression levels of genes of various biological functions were affected in response to the WT 3A alone (Fig. 8C and D), gene ontology (GO) analysis revealed that only genes related to protein trafficking and the UPR processes were differentially affected by the WT and mutant 3A proteins (Fig. 8E). Protein trafficking is a critical part of UPR, and the EV-A71 3A protein blocks the ER–Golgi transport (33). Additionally, our pilot test showed that Brefeldin A (BFA), a protein transportation inhibitor (Fig. 8F) that induces UPR (34), enhanced the mRNA and protein expression levels of BiP and XBP1s in a dose-dependent manner in RD cells (Fig. 8G and H). Thus, we speculated that the EV-A71 3A inhibited protein transport to induce UPR.

GBF1-mediated ARF1 activation is crucial for ER homeostasis

BFA targets guanine nucleotide exchange factors (GEF), such as BIG1, BIG2, GBF1, and the small GEF family (Fig. 9A). Among the GEFs, GBF1 is a key target of BFA in mammalian cells (35–37). Furthermore, GBF1 is a host factor involved in the replication of enteroviruses and interacts with 3A (38). Whether inhibition of GBF1 activates the UPR pathways is conflicting (39, 40), which led us to examine the correlation between GBF1 and UPR. Increased mRNA levels of BiP and XBP1s were observed in RD cells treated with the GBF1 inhibitor, Golgicide A (GCA) (Fig. 9A), in a dose-dependent manner (Fig. 9B). Similarly, GBF1 knockdown with siRNA induced the UPR pathway (Fig. 9C). GBF1 comprises multiple domains, including DCB, HUS, Sec7, HDS1, HDS2, and HDS3 domains (Fig. 9D). The inactive GBF1 that carries a substitution from glutamic acid to lysine at

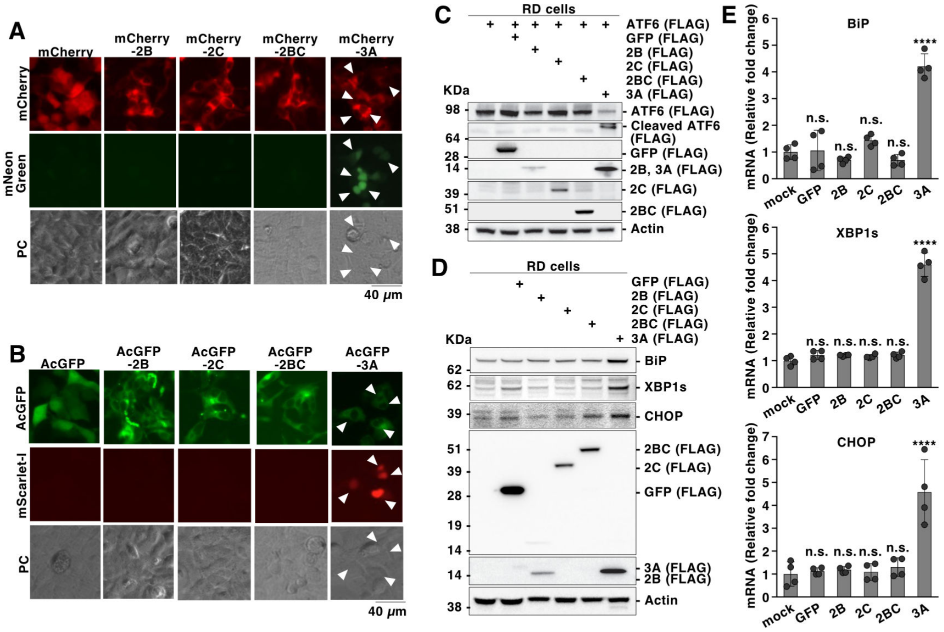

FIG 4 2B, 2C, or 2BC protein is not involved in UPR responses. (A) RD cells co-transfected with a plasmid encoding N-terminal mCherry-tagged 2B, 2C, 2BC, or 3A protein and the reporter vector. The fluorescent signals were detected using microscopy at 24 h post-transfection. Arrowhead: mNeonGreen-positive cells. The scale bar represents 40 μm. (B) RD cells co-transfected with a plasmid encoding N-terminal AcGFP-tagged 3A protein. The reporter vector and fluorescent signals were detected using microscopy at 24 h post-transfection. Arrowhead: mScarlet-I-positive cells. The scale bar represents 40 μm. (C) Expression levels of full-length ATF6, cleaved ATF6, GFP, 2B, 2C, 2BC, and 3A protein were detected using immunoblotting at 48 h post-transfection using an anti-FLAG antibody. (D) Expression of GFP, 2B, 2C, 2BC, 3A, BiP, XBP1s, and CHOP in RD cells was detected using immunoblotting. (E) Expression of BiP, XBP1s, or CHOP in RD cells expressing 2B, 2C, 2BC, or 3A was quantified using qPCR at 48 h post-transfection. The data presented in E denote mean ± S.D. of two independent experiments; data in A-D are representative of two independent experiments. For the experiment presented in E, significance (*****P* ≤ 0.00001; n.s., not significant) was determined using one-way ANOVA test (*n* = 4).

the 794th amino acid position (E794K) in the catalytic Sec7 domain (41) (Fig. 9D) induced the expression of BiP and XBP1s, but not the wildtype GBF1 (Fig. 9E and F). GBF1 activates the downstream protein, ARF1, to mediate protein transport. Expressing the inactive ARF1 that substituted threonine31 to asparagine (ARF1 T31N) (42) also induces the expression of *BiP* and *XBP1s* mRNA (Fig. 9G and H). These data suggest that the GBF1-ARF1 axis may regulate the UPR pathway.

We determined whether the recovery of ARF1 function under the suppression of GBF1 reduced UPRs. An ARF1 mutant with Gln71 substituted with Leu (Q71L) remains constitutively active even in the absence of GBF1 (42). Expression of ARF1 Q71L during GCA-mediated inhibition of GBF1 attenuated the expression of BiP or XBP1s (Fig. 9I and J). These data suggest that GBF1-mediated ARF1 activation is crucial for ER homeostasis and loss of GBF1 induces UPR.

3A protein sequesters GBF1 to induce the UPR pathways in EV-A71 infection

To determine whether the 3A protein induced the UPR through GBF1 and its downstream pathway, we co-expressed GBF1 or ARF1 Q71L with 3A in RD cells and observed a significantly reduced expression of BiP and XBP1s compared with those in the GFP control group (Fig. 10A). In contrast to GBF1, the expression of ACBD3, another major interacting partner of 3A protein (11, 12), did not affect the increased expression of BiP or XBP1s induced by the 3A protein (Fig. 10B). Moreover, 3A protein expression remained unaffected by the co-expression of either GBF1, ARF1 Q71L, or ACBD3 (Fig. 10C through E), denying the possibility that these proteins inhibit the expression of the 3A protein

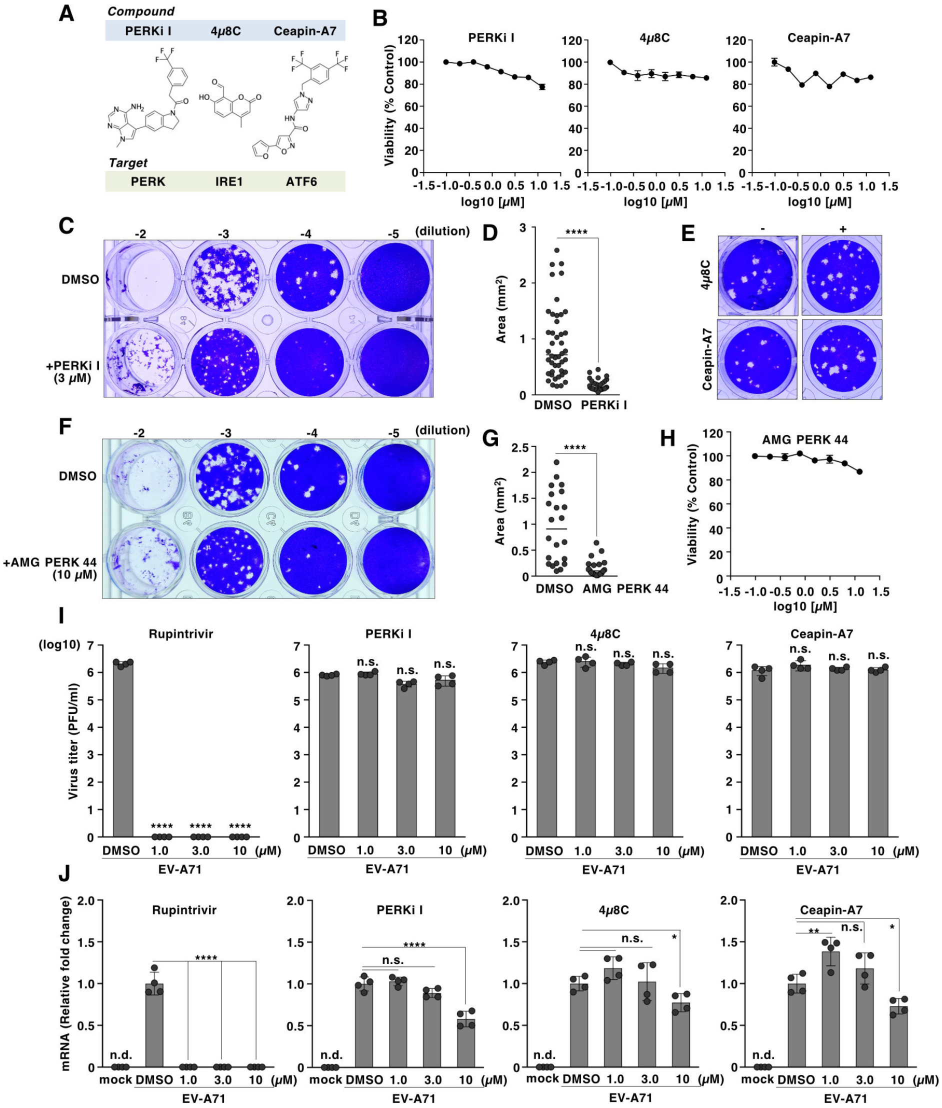

FIG 5 Inhibition of PERK reduces the plaque size of EV-A71. (A) The chemical structure of compounds used. (B) RD cells were treated with PERKi I, 4μ8C, or Ceapin-A7 for 96 h, and cell viability was determined by CellTiter-Glo (Promega). (C) Plaque morphology of EV-A71 in RD cells. The plaque overlay medium was supplemented with or without 3 μM of PERKi I. (D) Plaque overlay medium of RD cells infected with EV-A71 was supplemented with or without 3 μM of PERKi I, and plaque formation assay was performed in triplicate. The dilution of the viruses was 10^{-4}. All plaques presented in each well were analyzed, and their areas were quantified using Fiji software. (E) Plaque morphology of EV-A71-infected RD cells overlayed with medium supplemented with/without 3 μM of 4μ8c, or Ceapin-A7. The dilution of the viruses was 10^{-3}. (F) Plaque morphology of EV-A71 in RD cells. The plaque overlay medium was supplemented with or without 10 μM of AMG PERK 44. (G) The plaque overlay medium of EV-A71-infected RD cells was supplemented with or without 10 μM of AMG PERK 44, and plaque formation assay was performed in triplicate. The dilution of the viruses was 10^{-4}. All plaques in each well were analyzed, and their areas were quantified using Fiji software. (H) RD cells were treated with AMG PERK 44 for 96 h, and cell viability was determined by CellTiter-Glo (Promega). (I) RD cells infected with EV-A71 at an MOI of 0.3 were treated with PERKi I, 4μ8C, or Ceapin-A7 at concentrations of 1.0, 3.0, or 10 μM. Infectious titers in the culture supernatants were determined using a plaque-forming assay, and (J) intracellular EV-A71 RNA levels were determined using qPCR at 24 h post-infection. The data presented in I and J denote mean ± S.D. of two independent experiments; those in B–H are representative of two independent experiments. For the experiments presented in I and J, significance (*$P \leq 0.05$; **$P \leq 0.01$; ****$P \leq 0.00001$; n.s., not significant) was determined using one-way ANOVA test ($n = 4$). For the experiments presented in D and G, significance (****$P \leq 0.00001$) was determined using Student's *t*-test ($n = 3$).

itself. These data suggest that 3A expression induces UPR by impairing GBF1-mediated ARF1 function.

Subsequently, we examined the intracellular localization of GBF1, which is typically in the Golgi apparatus, and GM130, a marker of Golgi, upon EV-A71 infection. The localization of 3A protein in the infected cells was monitored using recombinant EV-A71 (14) expressing HA-tagged 3A protein (EV-A71-HA-3A). Although the localization of GM130 was disrupted upon infection (Fig. 10F), GBF1 was sequestered in the cytosolic structure, colocalizing with the 3A protein, as reported previously in CVB3 (43) (Fig. 10G and H). Moreover, 3D reconstitution of 3A-expressing RD cells revealed a structure similar to that observed in EV-A71-infected cells and indicated that GBF1 colocalized with EV-A71 3A (Fig. 10I).

The N-terminal region of GBF1 is responsible for interacting with the CVB3 3A protein (44). Therefore, we performed an *in silico* analysis of the potential interaction between the N-terminal fragments of GBF1 and EV-A71 3A protein. AlphaFold2 software reproduced the expected 3A structure, including the transmembrane helices (α3), the cytoplasmic N-terminal domain consisting of two helices (α1 and α2), and an intrinsically disordered region (12) (Fig. 11A). Moreover, the generated *in silico* structure indicated that I8 and I10 in the N-terminal disordered region of 3A were near the catalytic Sec7 domain of GBF1 (Fig. 11B).

Supporting the prediction by AlphaFold2 software, co-localization with GBF1 was not observed in RD cells co-expressing GBF1 together with either I8A or I10A mutant of 3A (Fig. 11C). Moreover, GBF1 can be pulled down by the wild-type 3A but not the I8A and I10A 3A mutants in cells co-expressing these proteins (Fig. 11D). Collectively, our data indicate that the I8 and I10 in the 3A protein are responsible for the interaction and sequestration of GBF1, having an essential role in activating UPR.

The observed localization of 3A protein in EV-A71-HA-3A-infected cells did not merge with the CANX, suggesting that its function in hijacking GBF1 indirectly affects ER homeostasis (Fig. 12A). Finally, we sought to determine the actual initiator of UPR during the sequestration of GBF1. UPR is typically initiated by the accumulation of proteins in the ER (45, 46). Since inhibition of protein transportation causes the concentration of some proteins to be localized in the ER (47), we examined the kinetics of the proteins typically localized in ER upon EV-A71 infection. Staining with the antibody against a common ER retention signal (Lys-Asp-Glu-Leu) revealed significant numbers of cytoplasmic foci in the infected cells (Fig. 12B) during EV-A71 infection (Fig. 12C). Our data indicate that the 3A-mediated sequestration of GBF1 causes the accumulated structures of ER-resident proteins, possibly associated with the initiation of UPR pathways. Collectively, our results suggest that the 3A protein sequesters GBF1 to impair the ARF1 activation and activates the PERK pathway of UPR, likely through the accumulation of proteins in the ER.

DISCUSSION

Data on the molecular mechanism underlying the enterovirus-induced UPR remain limited; therefore, this study clarified the virus-host interaction and showed that EV-A71 infection-induced ER remodeling, caused the accumulation of ER-resident proteins in the ER, and resulted in ER-dependent cell death through the PERK pathway. We also demonstrated that EV-A71 induced UPR by interacting with the host GBF1 via the viral 3A protein and that the Ile8 and Ile10 of the 3A are critical (Fig. 12D). Although the correlation between the GBF1 and the 3A protein was extensively studied, to our knowledge, this is the first report to characterize the role of the interaction between the two in the UPR.

Enteroviruses utilize GBF1 for viral replication, recruiting it to the RO through interaction with 3A (10, 43), and evade the immune system by inhibiting the transportation of immunoproteins, such as the cytokines or the major histocompatibility complex class I (16, 48–50). To better characterize the GBF1 involvement in the enterovirus pathogenesis, we investigated the significance of GBF1 on the UPR pathways. In line

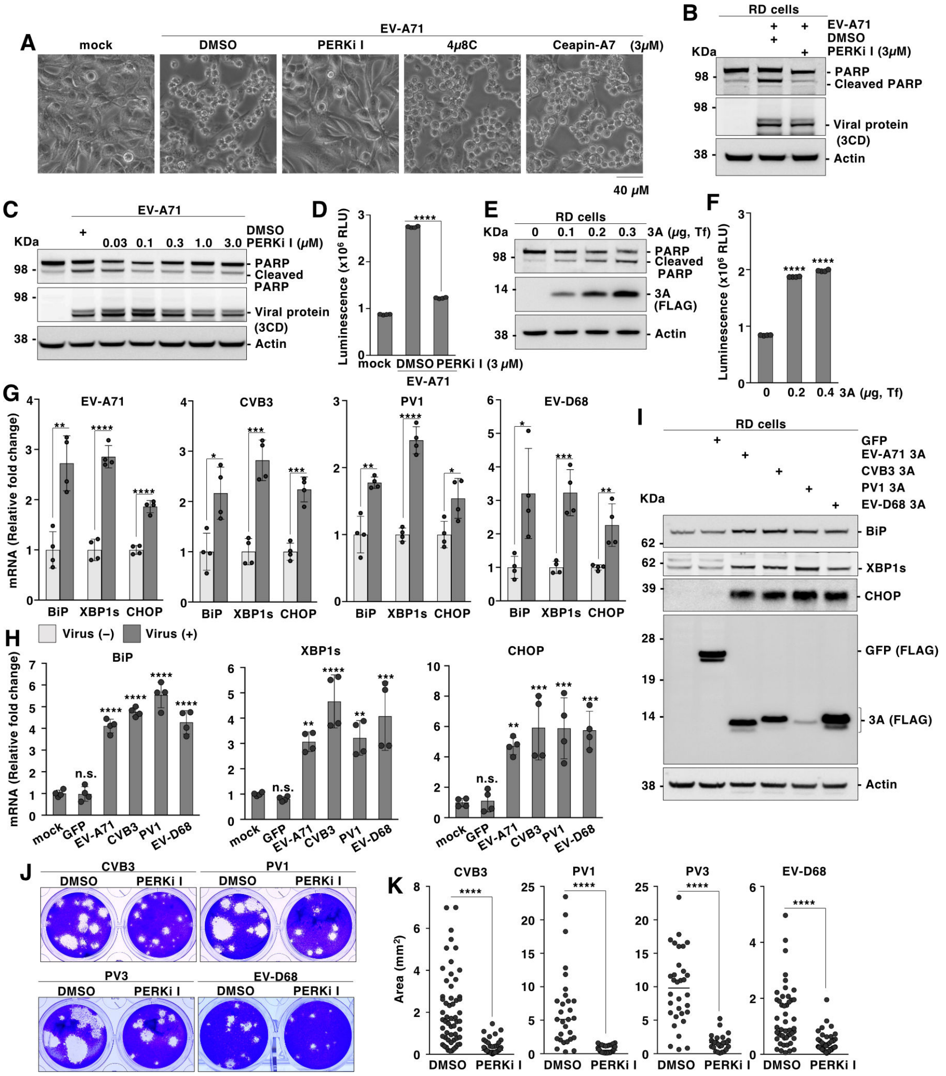

FIG 6 Enterovirus infection induces ER stress-dependent cell death. (A) RD cells infected with EV-A71 at an MOI of 0.3 were treated with 3 µM of PERKi I, 4µ8C, or Ceapin-A7 for 24 h, and phase contrast images were acquired using microscopy. The scale bar represents 40 µm. (B) RD cells infected with EV-A71 at an MOI of 0.3 were treated with 3 µM of PERKi I, and the expression of PARP and cleaved PARP was detected using immunoblotting at 24 h post-infection. (C) RD cells infected with EV-A71 at an MOI of 0.3 were treated with PERKi I at concentrations of 0.03, 0.1, 0.3, 1.0, or 3.0 µM, and the expression of PARP and cleaved PARP was detected using immunoblotting at 48 h post-transfection. (D) RD cells infected with EV-A71 at an MOI of 0.3 were treated with PERKi I at a concentration of 3 µM, and activity of caspase 3/7 was detected at 24 h post-transfection. (E). Expression of PARP and cleaved PARP in RD cells pre-transfected with various amounts of the 3A plasmids was detected using immunoblotting at 48 h post-transfection. (F) Caspase-3 and -7 activity in RD cells expressing varying levels of 3A protein was detected at 48 h post-transfection. (G) RD cells infected with EV-A71 or EV-D68 at an MOI of 0.1 were incubated for 36 h. RD cells infected with CVB3 or PV1 at an MOI of 0.01 were incubated for 18 h. Expression of BiP, XBP1s, and CHOP was quantified using qPCR. (H) RD cells expressing GFP or 3A proteins of enterovirus species (EV-A71, CVB3, PV1, and EV-D68). Expression of BiP, XBP1s, and CHOP was quantified using qPCR at 48 h post-transfection. (I) RD cells expressing GFP or 3A proteins of enterovirus species. Expression of BiP, XBP1s, and CHOP was detected using immunoblotting at 48 h post-transfection. (J) Plaque morphology of CVB3, PV1, PV3, and EV-D68 in RD cells. The plaque overlay medium was supplemented with or without 3 µM of PERKi I. Dilution of the viruses was 10^{-4} (CVB3), 10^{-7} (PV1), 10^{-7} (PV3), and 10^{-5} (EV-D68). (K) Plaque overlay medium of RD cells infected with CVB3, PV1, PV3, or EV-D68 was supplemented with or without 3 µM of PERKi I, and plaque formation assay was performed in triplicate. The dilution of the viruses was 10^{-4} (CVB3), 10^{-7} (PV1), 10^{-7} (PV3), and 10^{-5} (EV-D68). All plaques presented in each well were analyzed, and their areas were quantified using Fiji software. The transfected amounts of plasmid presented in each figure were calculated based on 24-well plates. The data presented in G

(Continued on next page)

FIG 6 (Continued)

and H denote the mean ± S.D. of two independent experiments; those in A–F and I–K are representative of two independent experiments. For the experiment presented in D, F, G, and H, significance (*$P \le 0.05$; **$P \le 0.01$; ***$P \le 0.001$; ****$P \le 0.00001$; n.s., not significant) was determined using one-way ANOVA test ($n = 4$). For the experiment presented in K, significance (****$P \le 0.00001$) was determined using Student's *t*-test ($n = 3$).

with a previous study showing that the siRNA-mediated GBF1 knockdown causes the UPR (39), we demonstrated that the function of the catalytic Sec7 domain of GBF1 is crucial for maintaining ER homeostasis. Expression of a constitutively active mutant of ARF1, a downstream effector of GBF1, alleviated the GBF1 inhibition-dependent UPR. Next, we demonstrated that hijacking the GBF1-ARF1 axis by the 3A protein caused the sequestration of GBF1, accumulation of ER-resident proteins, and induction of the UPR. Furthermore, treatment with the UPR inhibitor suppressed the virus-induced cytopathic effect. These data provide novel insights into controlling the viral UPR induced by GBF1 misfunction.

Consistent with previous reports, we confirmed that EV-A71, CVB3, PV, and EV-D68 activate the UPR (26, 28–30). Induction of UPR is therefore conserved among enterovirus species. Our data further indicated that the 3A proteins from all human enteroviruses induced UPR, suggesting that 3A proteins encoded in the genus *Enterovirus* led to UPR by hijacking GBF1. However, other viruses belonging to the family *Picornaviridae*, such as the Aichi virus, the foot-and-mouth disease virus (FMDV), and the Encephalomyocarditis virus (EMCV) replicate without utilizing GBF1 (51–54); FMDV and EMCV activate UPR (55, 56). Therefore, further studies remain warranted to characterize the UPR mechanisms among various families of *Picornaviridae.* Meanwhile, multiple viruses, including those belonging to the family *Flaviviridae, Reoviridae,* and *Coronaviridae,* utilize GBF1 for their propagation and induce UPR; therefore, the GBF1-dependent activation mechanism of viral UPR might apply to these viruses.

We identified two specific amino acid residues located at the 8th and 10th positions in the N-terminus of 3A of EV-A71 that are crucial in inducing the UPR through GBF1. GBF1 has been reported to support EV-A71 replication (57); however, its interacting domain with the 3A remains undetermined. Conversely, the role of the N-terminus of the 3A protein has been extensively characterized using CVB3 (10, 16, 44, 58). The Arg6, Glu7, Ile8, Lys9, or Ile10 in the 3A of CVB3 is responsible for the inhibition of protein trafficking (58) and substituting these amino acids to Ala abolished the interaction with GBF1 (10). Therefore, the functional domain of 3A protein is conserved in these enteroviruses, and our study highlights the association of the known function of 3A protein, such as blocking protein transport or interacting with GBF1, with a novel function, that is, the induction of UPR by enteroviruses. Additionally, we demonstrated that blocking protein transport by the 3A caused the accumulation of ER-resident proteins that are possible inducers of the enterovirus-driven UPR. Although we observed a substantial amount of ER-resident proteins accumulated in EV-A71-infected cells, it remains unclear whether the accumulation of specific proteins in ER is involved in initiating the UPR pathway. Additionally, the viral 3CD protein was also accumulated in the ER. Although we confirmed that the exogenous expression of 3CD protein alone could not induce UPR, the accumulated 3CD in enterovirus-infected cells may enhance viral UPR, which should be explored in future studies.

Excessive or prolonged UPR activates PERK/CHOP signaling, resulting in ER-dependent apoptosis. We revealed that the 3A protein can induce the PERK/CHOP-dependent apoptotic pathways during virus infection. Prior studies demonstrated that the enterovirus-encoded 2A or 3C proteins induced apoptosis through translational inhibition or cleavage of the hnRNP A1, respectively (59–61). We confirmed that the expression of 2A or 3C in RD cells did not activate the UPR, suggesting that the viral 2A or 3C proteins utilize a distinct pathway to induce apoptosis. Consistently, treatment with PERKi I efficiently, but not completely, suppressed cell death caused by the enterovirus infection. Therefore, it is reasonable to assume that the enterovirus utilizes multiple

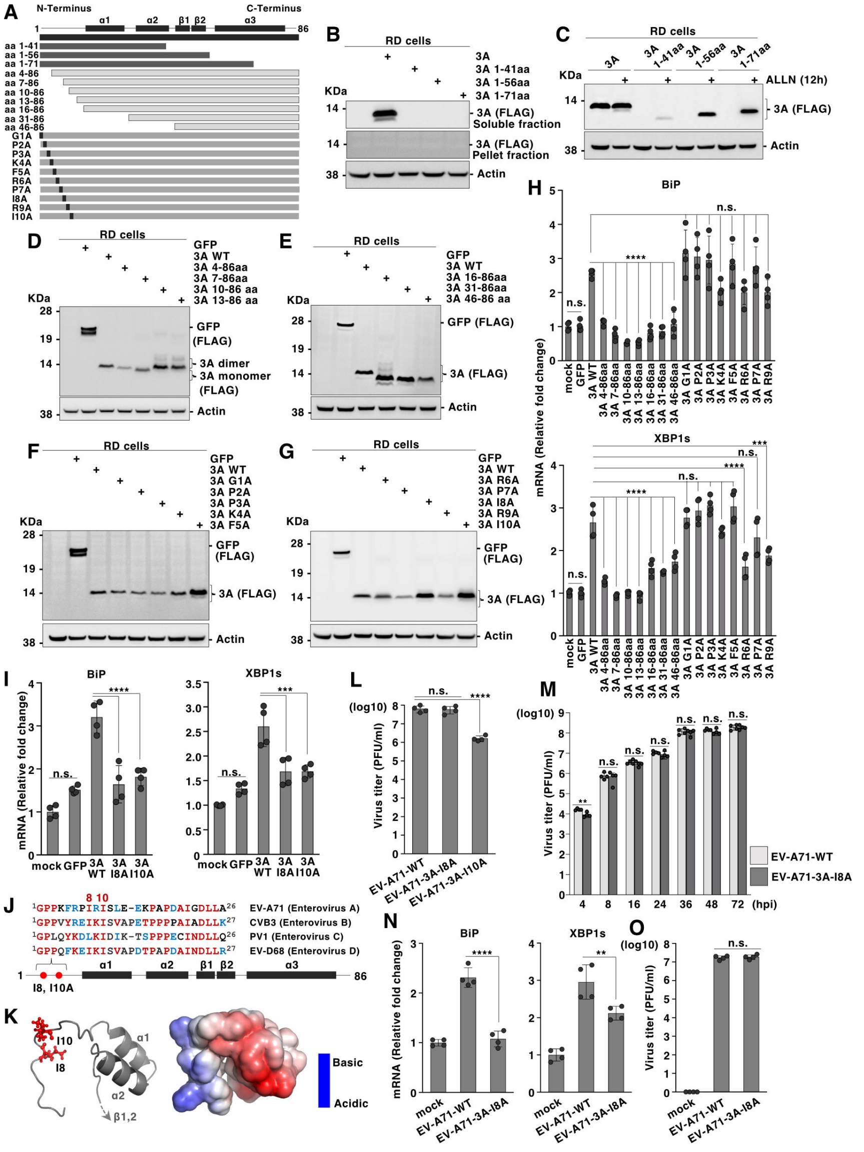

FIG 7 Role of Ile^{8} and Ile^{10} of the 3A protein in inducing UPR responses. (A) Schematic representation of the constructed mutant 3A proteins. (B) RD cells expressing C-terminal deletion mutants of 3A protein were lysed with 1% Triton X-100-containing lysis buffer, and both soluble and pellet fractions were subjected to immunoblotting. 3A protein was detected using an anti-FLAG antibody. (C) RD cells expressing 3A protein were subsequently treated with ALLN (proteasome inhibitor, 20 µM) for 12 h, and 3A protein was detected using immunoblotting. (D-G) RD cells expressing mutant 3A proteins were subjected to immunoblotting at 48 h post-transfection. (H) Expression of BiP and XBP1s in RD cells expressing wild-type or mutants of 3A was quantified using qPCR at 48 h post-transfection. (I) Expression of BiP or XBP1s in RD cells expressing wild-type or mutants of 3A protein was quantified using qPCR at 48 h post-transfection. (J) The N-terminal amino acid sequence of 3A proteins of enterovirus species (EV-A71, CVB3, PV1, and EV-D68) was aligned using Clustal Omega (*upper*). Secondary structures of 3A protein derived from EV-A71 were indicated. Information on the secondary structures was obtained from Protein Data Bank (PDB ID code: 6HLW) and a related article (PMID: 31381608) (*Lower*). (K) Homology modeling of the N-terminal region of 3A protein was performed using the Iterative Threading ASSEmbly Refinement (I-TASSER) server. The structure of the 3A protein is shown with a cartoon backbone representation (*Left*) and electrostatic surface representation (*Right*). (L) Infectious titers of the non-passaged EV-A71-I8A or EV-A71-I10A produced in RD cells were determined using a plaque-forming assay. (M) RD cells were infected with EV-A71-3A-I8A at an MOI of 0.1, and infectious

(Continued on next page)

FIG 7 (Continued)

titers were determined using a plaque-forming assay at 4, 8, 16, 24, 36, 48, or 72 h post-infection. (N) Expression of BiP (*Left*) and XBP1s (*Right*) in RD cells infected with EV-A71 at an MOI of 0.1 was determined using qPCR at 36 h post-infection. (O) The infectious titers of EV-A71 and EV-A71-3A-I8A obtained from the experiment presented in Fig. 7N were determined using a plaque-forming assay. The data shown in H, I, and L-O are the mean S.D. of two independent experiments; those in B-G are representative of two independent experiments. Significance (***P* ≤ 0.01; ****P* ≤ 0.001; *****P* ≤ 0.00001; n.s., not significant) was determined using one-way ANOVA test (*n* = 4).

pathways to cause cell death. The significance of each pathway during the viral infection should be clarified via comprehensive studies in the future.

Interestingly, 3A protein can suppress 2A-mediated apoptosis by preventing the transportation of TNFα receptors to the cell surface (50). Thus, prevention of protein transportation acts as a double-edged sword for cells by inhibiting and inducing apoptosis. Considering the life cycle of the enterovirus, the 3A protein may initially prevent 2A-mediated apoptosis for efficient replication, which culminates in critical disruption of ER homeostasis, triggering apoptosis at the late stage of infection.

Among the pathways involved in ER homeostasis, the 3A protein activates the PERK-mediated signaling pathway that triggers ER stress-dependent apoptotic cell death. Although the pharmaceutical inhibition of PERK exerted no impact on the virus titers and viral RNA replication, we revealed that the inhibition of PERK broadly inhibited the apoptosis caused by a wide range of human enteroviruses. Therefore, the significance of PERK in enterovirus infection is highlighted mainly in virus-induced apoptotic events. The PERK/CHOP signaling is involved in the pathogenesis of several positive-stranded RNA viruses. For instance, the PERK signaling contribution to the disease severity of infection by the Middle East Respiratory Syndrome coronavirus and Japanese encephalitis virus (JEV)-induced apoptosis depends on the PERK signaling, and the pathogenesis and survival of the infected mice (21, 23). Furthermore, BCL-XL, an anti-apoptotic BCL-2 family member regulated by CHOP, is a therapeutic target against JEV (62). Over 110 viruses, categorized as human enterovirus, cause various diseases and severe neurological symptoms. The enteroviral infection causes viremia that triggers the entry and propagation of the virus in neural cells, irreversibly damaging the host cells. Although viral entry receptors and host factors vary among enterovirus species, characterizing the mechanisms by which apoptosis caused by GBF1-mediated UPR contributes to neurological pathogenesis is essential for developing host-directed therapy to alleviate symptoms of various enteroviral infections.

Collectively, our results demonstrate that GBF1 plays a crucial role in enterovirus-induced UPR, and 3A protein hijacks and sequesters GBF1 to facilitate vital replication, simultaneously suppressing the original function of GBF1. Furthermore, we found that enterovirus-infected cells exhibited characteristic ER structures and accumulation of ER-residue proteins and elucidated the mechanism underlying the disruption of ER homeostasis induced by enterovirus infection to affect cell fate. Notably, the activation of PERK/CHOP signaling induced apoptosis, which was commonly observed in cells infected with EV-A71, CVB3, PV, and EV-D68. This study illustrated a viral hijacking machinery of cellular proteins linked to the pathogenic mechanism of common human enteroviruses.

MATERIALS AND METHODS

Cell lines and viruses

Human rhabdomyosarcoma cell lines (RD) were obtained from the US Centers for Disease Control. The human embryonic kidney cell line (HEK293T), human colorectal adenocarcinoma (HT-29), and human cervical carcinoma cell line (HeLa) were obtained from the National Institute of Infectious Disease, Tokyo, Japan. All cell lines were maintained in

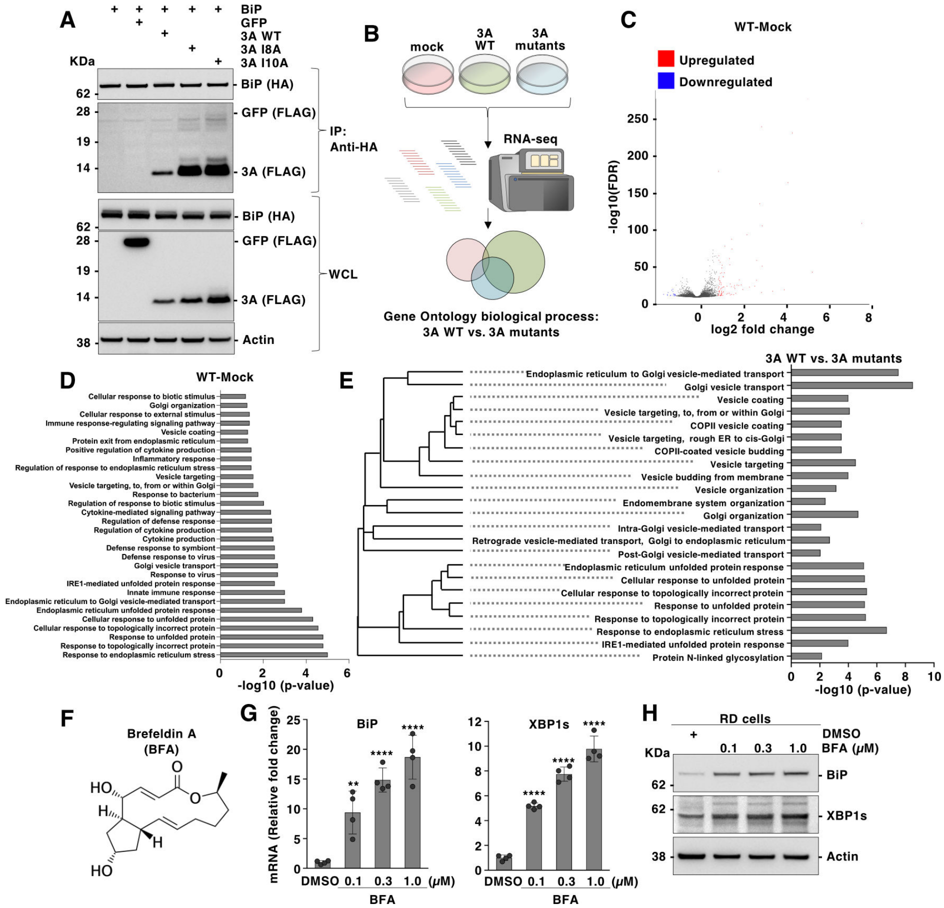

FIG 8 Role of Ile^{8} and Ile^{10} of the 3A protein in UPR induction and protein transportation. (A) HEK293T cells co-expressing HA-tagged BiP with FLAG-tagged GFP, FLAG-tagged wild type or mutants of 3A were immunoprecipitated and subjected to sodium dodecyl sulfate-polyacrylamide gel electrophoresis and immunoblotting. (B) Schematic representation of RNA-seq performed. RD cells expressing wild-type or mutants of 3A protein were analyzed. (C) Volcano plots depicting the differentially expressed genes (DEGs). RD cells and 3A-expressing RD cells were compared. (D) Gene ontology (GO) biological process of RD cells and 3A-expressing RD cells were compared using Integrated Differential Expression and Pathway (iDEP) analysis. All biological processes demonstrated significant differences. (E) Gene ontology (GO) biological process of RD cells expressing wild type or mutants 3A protein was compared using iDEP analysis. All biological processes that showed significant differences were shown. (F) Chemical structure of Brefeldin A (BFA). Expression of BiP and XBP1s in RD cells treated with BFA (0.1, 0.3, and 1.0 µM) for 24 h was quantified using qPCR (G) and immunoblotting (H). The data presented in G denote mean ± S.D. of two independent experiments; those in A and H are representative of two independent experiments. Significance (***P* ≤ 0.01; *****P* ≤ 0.00001; n.s., not significant) was determined using one-way ANOVA test (*n* = 4).

Dulbecco's Modified Eagle Medium (DMEM; High Glucose) with L-Glutamine and Phenol Red (Wako, 044–29765) supplemented with 10% fetal bovine serum (FBS), 100 U/mL penicillin, and 100 µg/mL streptomycin. The isolated strain of EV-A71 (strain SK-EV006) were generated using the DNA-based reverse genetics system for EV-A71, as previously described (63, 64). pcDNA3 vector containing EV-A71 full genome was transfected in RD cells, and the infectious viruses were collected at 3 days post-transfection. PV (strain, Sabin1, and Sabin3) was obtained from the Department of Microbiology and Immunology, University of California. The isolated strain of CVB3 (strain Kandolf) was generated from pcDNA CVB3 (Addgene, #158645), as described in a previous study with slight modifications (65). Subsequently, it was serially passaged in RD cells to allow adaptation to the cells (66) before using them in the experiments (Fig. 6G, J, and K). The reference strain of EV-D68 (strain Fermon) was obtained from the Institute Pasteur. EV-A71-3A-HA, EV-A71-3A-I8A, or EV-A71-3A-I10A was generated using the DNA-based reverse genetics

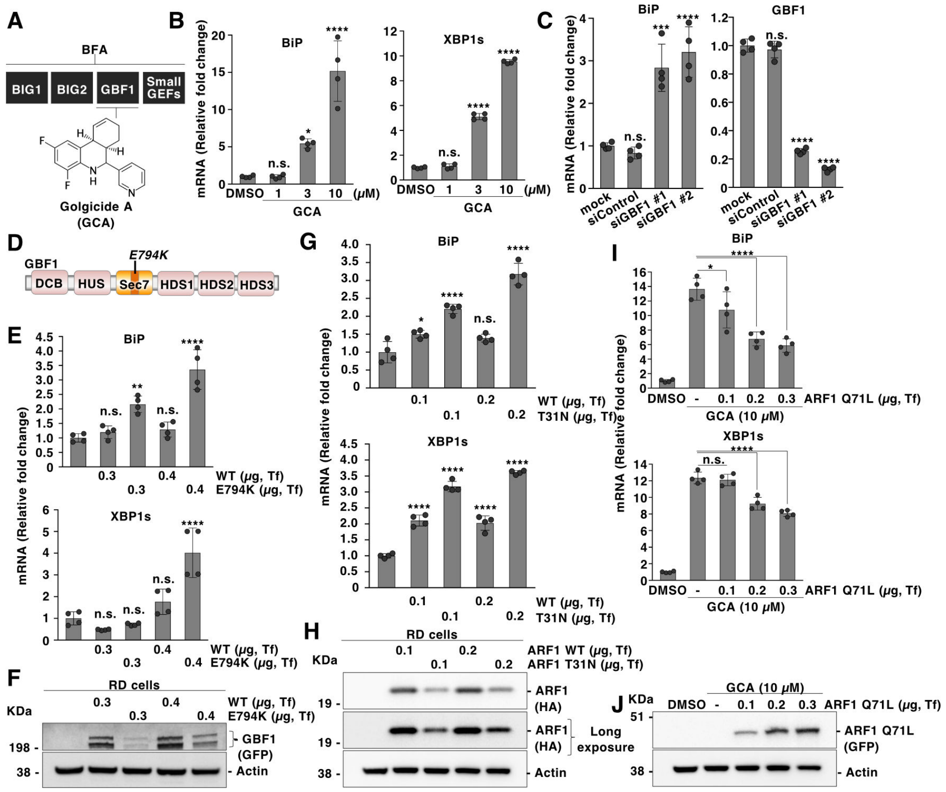

FIG 9 GBF1-induced ARF1 activation is crucial for ER homeostasis. (A) Schematic representation of inhibitors used in this study and their targets. BFA broadly targets GEF families, whereas Golgicide A (GCA) specifically targets GBF1. (B) Expression of BiP (*Left*) and XBP1s (*Right*) in GCA-treated RD cells (1, 3, 10 μM) for 24 h was quantified using qPCR. (C) Expression of BiP (*Left*) or GBF1 (*Right*) in RD or GBF1-knockdown RD cells was quantified using qPCR. (D) Schematic representation of the domain structure of GBF1. The E794K mutation introduced in GBF1 is located in the Sec7 domain. (E) Expression of BiP (*Upper*) and XBP1s (*lower*) in RD cells transfected with wild type or E794K mutant of GBF1 was quantified using qPCR at 48 h post-transfection. (F) Expression of GBF1 in RD cells transfected with wild type or E794K mutant of GBF1 was confirmed using immunoblotting at 48 h post-transfection. (G) Expression of BiP (*Upper*) and XBP1s (*Lower*) in RD cells transfected with wild type or T31N mutant of ARF1 was quantified using qPCR at 48 h post-transfection. (H) Expression of ARF1 in RD cells transfected with wild type or T31N mutant of ARF1 was assessed using immunoblotting at 48 h post-transfection. (I) RD cells expressing ARF1 Q71L at varying levels were treated with GCA (10 μM) 24 h post-transfection. The expression of BiP (*Upper*) and XBP1s (*Lower*) was quantified using qPCR at 48 h post-transfection. (J) RD cells expressing ARF1 Q71L at varying levels were treated with GCA (10 μM) 24 h post-transfection. The expression of ARF1 was detected using immunoblotting at 48 h post-transfection. The amount of the transfected plasmids presented in each figure was calculated based on 24-well plates. The data presented in B, C, E, G, and I denote mean ± S.D. of two independent experiments; those in F, H, and J are representative of two independent experiments. Significance (*$P \leq 0.05$; **$P \leq 0.01$; ***$P \leq 0.001$; ****$P \leq 0.00001$; n.s., not significant) was determined using one-way ANOVA test ($n = 4$).

system for EV-A71. The HA-tag was inserted after the amino acid residue Pro^2 in the 3A protein (67).

Antibodies and reagents

The following antibodies and reagents were purchased from the sources indicated: Enterovirus 71 2B antibody (GTX132343; GeneTex), Enterovirus 71 2C antibody (GTX132354; GeneTex), Enterovirus 71 3AB antibody (GTX132344; GeneTex), Enterovirus 71 3CD antibody (GTX132355; GeneTex), Anti-Calnexin monoclonal antibody (M178-3; MBL Life science), Anti-Calnexin pAb (PM060; MBL Life science), Anti-KDEL monoclonal antibody (M181-3; MBL Life science), Anti-GM130 monoclonal antibody (M179-3; MBL Life science), PDI monoclonal antibody (66422-1-Ig; Proteintech), GRP78/BIP polyclonal

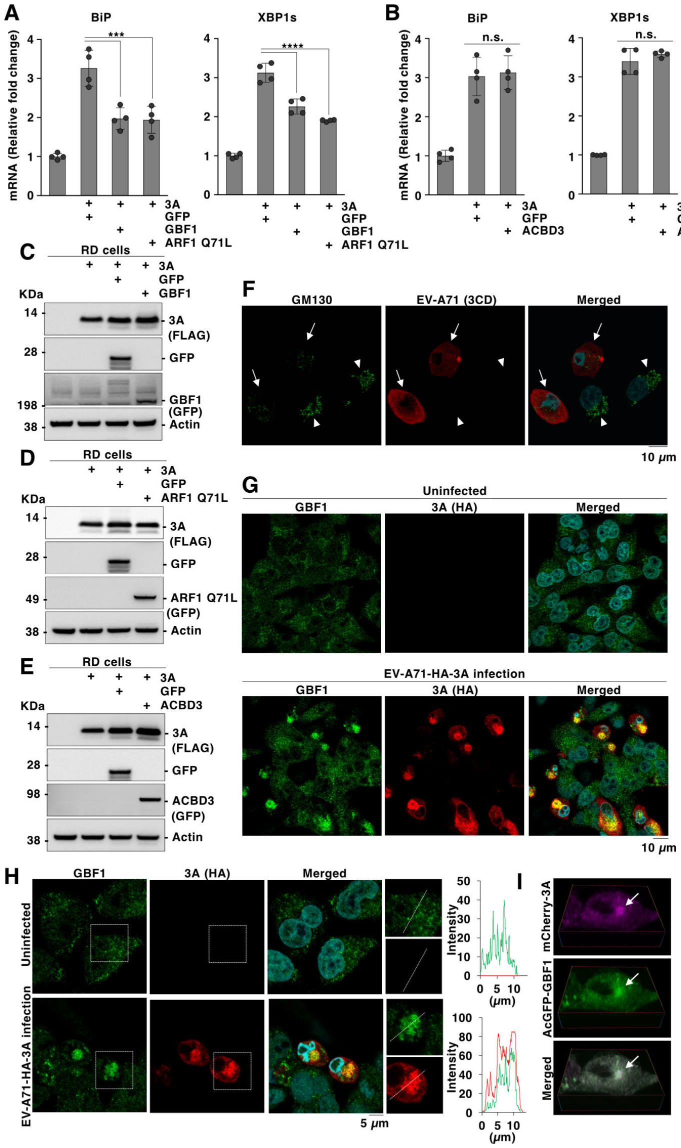

FIG 10 3A protein sequesters GBF1 in the cytosolic structure and induces UPR. (A) Expression of BiP and XBP1s in RD cells co-expressing 3A protein with either GFP, GBF1, or ARF1 Q71L was quantified using qPCR at 48 h post-transfection. (B) Expression of BiP and XBP1s in RD cells co-expressing 3A protein with either GFP or ACBD3 was quantified using qPCR at 48 h post-transfection. (C) RD cells co-expressing 3A with GFP or GBF1 were subjected to immunoblotting at 48 h post-transfection. (D) RD cells co-expressing 3A with GFP or ARF1 Q71L were subjected to immunoblotting at 48 h post-transfection. (E) RD cells co-expressing 3A with GFP or ACBD3 were subjected to immunoblotting at 48 h post-transfection. (F) RD cells infected with EV-A71 at an MOI of 0.3 were stained with anti-GM130 antibody, anti-EV-A71 3CD antibody, and DAPI at 30 h post-infection, and fluorescent signals were detected using microscopy. Arrowhead and straight arrow denote uninfected and EV-A71-infected cells, respectively. The scale bar represents 10 µm. (G) RD cells infected with EV-A71 expressing HA-tagged 3A protein (EV-A71-HA-3A) at an MOI of 0.3 were stained with anti-GBF1 antibody, anti-HA antibody, and DAPI at 24 h post-infection, and fluorescent signals were detected using microscopy. The scale bar represents 10 µm. (H) RD cells infected with recombinant EV-A71-HA-3A at an MOI of 0.3 were stained with anti-GBF1 antibody, anti-HA antibody, and DAPI at 24 h post-infection, and fluorescent signals were detected using microscopy. The scale bar represents 5 µm. The colocalization analysis was performed using Fiji software (*Right*). (I) RD cells co-expressing N-terminal mCherry-tagged 3A protein with N-terminal AcGFP-tagged GBF1 were examined using fluorescent microscopy at 48 h post-transfection. 3d reconstitution was performed

(Continued on next page)

FIG 10 (Continued)

using the cellSens imaging software (OLYMPUS). The arrows indicate the co-localization of GBF1 and 3A proteins. The data presented in A and B denote mean ± S.D. of two independent experiments; those in C-I are representative of two independent experiments. Significance (***$P \leq 0.001$; ****$P \leq 0.00001$; n.s., not significant) was determined using one-way ANOVA test ($n = 4$).

antibody (11587-1-AP; Proteintech), XBP1S-specific polyclonal antibody (24868-1-AP; Proteintech), CHOP; GADD153 polyclonal antibody (15204-1-AP; Proteintech), PARP antibody #9542 (9542S; Cell Signaling), Living Colors A.v. monoclonal antibody (JL-8) (CAT#632381; Clontech), GBF1 polyclonal antibody (25183–1-AP; Proteintech), Alexa Fluor (AF) 488-conjugated anti-mouse IgG antibodies (A-11001; Life Technologies), AF488-conjugated anti-rabbit IgG antibodies (A-11008; Life Technologies), AF594-conjugated anti-mouse IgG antibodies (A-11032; Life Technologies), AF594-conjugated anti-rabbit IgG antibodies (A-11037; Life Technologies), anti-FLAG M2-Peroxidase (HRP) monoclonal antibody produced in mouse (A8592; Merck), Anti-HA-tag mAb (M180-3; MBL Life science), anti-β-Actin monoclonal antibody produced in mouse (A2228; Merck), Peroxidase AffiniPure Goat anti-mouse IgG (H + L) (115-035-003; Jackson Immuno Research Laboratories, Inc.), Peroxidase AffiniPure Goat anti-Rabbit IgG (H + L) (111-035-003; Jackson Immuno Research Laboratories, Inc.), InSolution™ PERK Inhibitor I, GSK2606414 - CAS 1337531-89-1 - Calbiochem (508340; Merck), 4μ8C (HY-19707; MedChemExpress), Ceapin-A7 (SML2330; Merck), AMG PERK 44 (SML3049; Merck), (+)-Brefeldin A (BVT-0190; AdipoGen LIFE SCIENCES), and Golgicide A (HY-100540; MedChemExpress).

Plasmids

pLVX-XBP1 mNeonGreen NLS and pLVX-ATF4 mScarlet NLS were gifts from David Andrews (Addgene plasmid #115968; http://n2t.net/addgene:115968; RRID:Addgene_115968 and Addgene plasmid #115969; http://n2t.net/addgene:115969; RRID:Addgene_115969). pcDNA CVB3 was a gift from Kevin Janes (Addgene plasmid #158645; http://n2t.net/addgene:158645; RRID:Addgene_158645). All the plasmid vectors used in this study are listed in Table 1. The Tks Gflex DNA Polymerase (Takara-Bio) was used to amplify all complementary DNAs (cDNAs). The amplified cDNAs were cloned into linearized vectors using an In-Fusion HD cloning kit (Clontech) or In-Fusion Snap Assembly Master Mix (Clontech). The sequences of all the plasmids have been confirmed using SeqStudio Genetic Analyzer (Thermo Fisher Scientific), and they were transfected into cells using *Trans*IT-LT1 Transfection Reagent (Mirus).

Quantitative RT-PCR (qPCR)

Total RNAs were prepared using ISOGEN II (Nippon Gene) according to the manufacturer's protocol. The extracted RNAs were then used to synthesize cDNAs by a High-Capacity RNA-to-cDNA kit (Applied Biosystems), according to the manufacturer's protocol. The mRNA levels of *BiP*, *XBP1s*, *CANX*, *GRP94*, *PDI*, *EDEM1*, *HERPD1*, *CHOP*, *EV-A71,* and *GBF1* were determined using Fast SYBR Green Master Mix (Thermo Fisher Scientific) and Applied Biosystems 7500 Fast (Thermo Fisher Scientific), QuantStudio 3 (Thermo Fisher Scientific), or QuantStudio 5 Real-Time PCR Systems (Thermo Fisher Scientific). The ddCt method was used to quantify the amount of each mRNA using *GAPDH* as an internal control. The following primers were used: *GAPDH* 5′-TGTAGTTGAGGTCAATGAAGGG-3′ and 5′-ACATCGCTCAGACACCATG-3′; *BiP* 5′-CGAGGAGGAGGACAAGAAGG-3′ and 5′-CACCTTGAACGGCAAGAACT-3′; *XBP1s* 5′-TGCTGAGTCCGCAGCAGGTG-3′ and 5′-GCTGGCAGGCTCTGGGGAAG-3′; *CANX* 5′-GCTGGTTAGATGATGAGCCTGAG-3′ and 5′-ACACCACATCCAGGAGCTGACT-3′; *GRP94* 5′-GGAGAGTCGTGAAGCAGTTGAG-3′ and 5′-CCACCAAAGCACACGGAGATTC-3′; *PDI* 5′-GGAATGGAGACACGGCTTC-3′ and 5′-TTCAGCCAGTTCACGATGTC-3′; *EDEM1* 5′-ACGAGCAGTGAAAGCCCTTTGG-3′ and 5′-CCACTCTGCTTTCCAACCCAGT-3′; *HERPD1* 5′-CCAATGTCTCAGGGACTTGCTTC-3′ and 5′-CGATTAGAACCAGCAGG

TABLE 1 List of plasmids used in this study

Plasmid name	Genes expressed in cell lines	cDNA (ORFs) Sources	Epitope tags	Cloning vectors (Sources)
pLVX-XBP1 mNeonGreen NLS	XBP1s, mNeonGreen NLS	-	-	Addgene (#115968)
pLVX-ATF4 mScarlet NLS	ATF4, mScarlet NLS	-	-	Addgene (#115969)
pcDNA CVB3	CVB3	-	-	Addgene (#158645)
pCAGGS FLAG-GFP	eGFP	-	N-terminus FLAG	pCAGGS
pCAGGS FLAG-VP1	EV-A71 VP1 (strain SK-EV006)	EV-A71 cDNA (strain SK-EV006)	N-terminus FLAG	pCAGGS
pCAGGS FLAG-VP2	EV-A71 VP2 (strain SK-EV006)	EV-A71 cDNA (strain SK-EV006)	N-terminus FLAG	pCAGGS
pCAGGS FLAG-VP3	EV-A71 VP3 (strain SK-EV006)	EV-A71 cDNA (strain SK-EV006)	N-terminus FLAG	pCAGGS
pCAGGS FLAG-VP4	EV-A71 VP4 (strain SK-EV006)	EV-A71 cDNA (strain SK-EV006)	N-terminus FLAG	pCAGGS
pCAGGS FLAG-VP0	EV-A71 VP0 (strain SK-EV006)	EV-A71 cDNA (strain SK-EV006)	N-terminus FLAG	pCAGGS
pCAGGS FLAG-2A	EV-A71 2A (strain SK-EV006)	EV-A71 cDNA (strain SK-EV006)	N-terminus FLAG	pCAGGS
pCAGGS FLAG-2B	EV-A71 2B (strain SK-EV006)	EV-A71 cDNA (strain SK-EV006)	N-terminus FLAG	pCAGGS
pCAGGS FLAG-2C	EV-A71 2C (strain SK-EV006)	EV-A71 cDNA (strain SK-EV006)	N-terminus FLAG	pCAGGS
pCAGGS FLAG-3A	EV-A71 3A (strain SK-EV006)	EV-A71 cDNA (strain SK-EV006)	N-terminus FLAG	pCAGGS
pCAGGS FLAG-3B	EV-A71 3B (strain SK-EV006)	EV-A71 cDNA (strain SK-EV006)	N-terminus FLAG	pCAGGS
pCAGGS FLAG-3C	EV-A71 3C (strain SK-EV006)	EV-A71 cDNA (strain SK-EV006)	N-terminus FLAG	pCAGGS
pCAGGS FLAG-3D	EV-A71 3D (strain SK-EV006)	EV-A71 cDNA (strain SK-EV006)	N-terminus FLAG	pCAGGS
pCAGGS FLAG-2BC	EV-A71 2BC (strain SK-EV006)	EV-A71 cDNA (strain SK-EV006)	N-terminus FLAG	pCAGGS
pCAGGS FLAG-3AB	EV-A71 3AB (strain SK-EV006)	EV-A71 cDNA (strain SK-EV006)	N-terminus FLAG	pCAGGS
pCAGGS FLAG-3CD	EV-A71 3CD (strain SK-EV006)	EV-A71 cDNA (strain SK-EV006)	N-terminus FLAG	pCAGGS
pCAGGS FLAG-3A (aa 1–41)	EV-A71 3A (aa 1–41) (strain SK-EV006)	pCAGGS FLAG-3A	N-terminus FLAG	pCAGGS
pCAGGS FLAG-3A (aa 1–56)	EV-A71 3A (aa 1–56) (strain SK-EV006)	pCAGGS FLAG-3A	N-terminus FLAG	pCAGGS
pCAGGS FLAG-3A (aa 1–71)	EV-A71 3A (aa 1–71) (strain SK-EV006)	pCAGGS FLAG-3A	N-terminus FLAG	pCAGGS
pCAGGS FLAG-3A (aa 4–86)	EV-A71 3A (aa 4–86) (strain SK-EV006)	pCAGGS FLAG-3A	N-terminus FLAG	pCAGGS
pCAGGS FLAG-3A (aa 7–86)	EV-A71 3A (aa 7–86) (strain SK-EV006)	pCAGGS FLAG-3A	N-terminus FLAG	pCAGGS
pCAGGS FLAG-3A (aa 10–86)	EV-A71 3A (aa 10–86) (strain SK-EV006)	pCAGGS FLAG-3A	N-terminus FLAG	pCAGGS
pCAGGS FLAG-3A (aa 13–86)	EV-A71 3A (aa 13–86) (strain SK-EV006)	pCAGGS FLAG-3A	N-terminus FLAG	pCAGGS
pCAGGS FLAG-3A (aa 16–86)	EV-A71 3A (aa 16–86) (strain SK-EV006)	pCAGGS FLAG-3A	N-terminus FLAG	pCAGGS
pCAGGS FLAG-3A (aa 31–86)	EV-A71 3A (aa 31–86) (strain SK-EV006)	pCAGGS FLAG-3A	N-terminus FLAG	pCAGGS
pCAGGS FLAG-3A (aa 46–86)	EV-A71 3A (aa 46–86) (strain SK-EV006)	pCAGGS FLAG-3A	N-terminus FLAG	pCAGGS
pCAGGS FLAG-3A (G1A)	EV-A71 3A (G1A) (strain SK-EV006)	pCAGGS FLAG-3A	N-terminus FLAG	pCAGGS
pCAGGS FLAG-3A (P2A)	EV-A71 3A (P2A) (strain SK-EV006)	pCAGGS FLAG-3A	N-terminus FLAG	pCAGGS
pCAGGS FLAG-3A (P3A)	EV-A71 3A (P3A) (strain SK-EV006)	pCAGGS FLAG-3A	N-terminus FLAG	pCAGGS
pCAGGS FLAG-3A (K4A)	EV-A71 3A (K4A) (strain SK-EV006)	pCAGGS FLAG-3A	N-terminus FLAG	pCAGGS
pCAGGS FLAG-3A (F5A)	EV-A71 3A (F5A) (strain SK-EV006)	pCAGGS FLAG-3A	N-terminus FLAG	pCAGGS
pCAGGS FLAG-3A (R6A)	EV-A71 3A (R6A) (strain SK-EV006)	pCAGGS FLAG-3A	N-terminus FLAG	pCAGGS

(*Continued on next page*)

TABLE 1 List of plasmids used in this study (*Continued*)

Plasmid name	Genes expressed in cell lines	cDNA (ORFs) Sources	Epitope tags	Cloning vectors (Sources)
pCAGGS FLAG-3A (P7A)	EV-A71 3A (P7A) (strain SK-EV006)	pCAGGS FLAG-3A	N-terminus FLAG	pCAGGS
pCAGGS FLAG-3A (I8A)	EV-A71 3A (I8A) (strain SK-EV006)	pCAGGS FLAG-3A	N-terminus FLAG	pCAGGS
pCAGGS FLAG-3A (R9A)	EV-A71 3A (R9A) (strain SK-EV006)	pCAGGS FLAG-3A	N-terminus FLAG	pCAGGS
pCAGGS FLAG-3A (I10A)	EV-A71 3A (I10A) (strain SK-EV006)	pCAGGS FLAG-3A	N-terminus FLAG	pCAGGS
pCAGGS mCherry	mCherry	-	-	pCAGGS
pCAGGS mCherry-3A	EV-A71 3A (strain SK-EV006)	pCAGGS FLAG-3A	N-terminus mCherry	pCAGGS
pCAGGS mCherry-3A (I8A)	EV-A71 3A (I8A) (strain SK-EV006)	pCAGGS FLAG-3A	N-terminus mCherry	pCAGGS
pCAGGS mCherry-3A (I10A)	EV-A71 3A (I10A) (strain SK-EV006)	pCAGGS FLAG-3A	N-terminus mCherry	pCAGGS
pCAGGS mCherry-2B	EV-A71 2B (strain SK-EV006)	EV-A71 cDNA (strain SK-EV006)	N-terminus mCherry	pCAGGS
pCAGGS mCherry-2C	EV-A71 2C (strain SK-EV006)	EV-A71 cDNA (strain SK-EV006)	N-terminus mCherry	pCAGGS
pCAGGS mCherry-2BC	EV-A71 2BC (strain SK-EV006)	EV-A71 cDNA (strain SK-EV006)	N-terminus mCherry	pCAGGS
pCAGGS AcGFP	AcGFP	-	-	pCAGGS
pCAGGS AcGFP-3A	EV-A71 3A (strain SK-EV006)	pCAGGS FLAG-3A	N-terminus AcGFP	pCAGGS
pCAGGS AcGFP-2B	EV-A71 2B (strain SK-EV006)	EV-A71 cDNA (strain SK-EV006)	N-terminus AcGFP	pCAGGS
pCAGGS AcGFP-2C	EV-A71 2C (strain SK-EV006)	EV-A71 cDNA (strain SK-EV006)	N-terminus AcGFP	pCAGGS
pCAGGS AcGFP-2BC	EV-A71 2BC (strain SK-EV006)	EV-A71 cDNA (strain SK-EV006)	N-terminus AcGFP	pCAGGS
pCAGGS One-Strep-FLAG (OSF)-eGFP	eGFP	-	N-terminus OSF	pCAGGS
pCAGGS OSF-3A	EV-A71 3A (strain SK-EV006)	pCAGGS FLAG-3A	N-terminus OSF	pCAGGS
pCAGGS OSF-3A (I8A)	EV-A71 3A (I8A) (strain SK-EV006)	pCAGGS FLAG-3A	N-terminus OSF	pCAGGS
pCAGGS OSF-3A (I10A)	EV-A71 3A (I10A) (strain SK-EV006)	pCAGGS FLAG-3A	N-terminus OSF	pCAGGS
pCAGGS FLAG-3A (CVB3)	CVB3 3A (strain Kandorf)	CVB3 cDNA (strain Kandorf)	N-terminus FLAG	pCAGGS
pCAGGS FLAG-3A (PV1)	PV1 3A (strain Sabin1)	PV1 cDNA (strain Sabin1)	N-terminus FLAG	pCAGGS
pCAGGS FLAG-3A (EV-D68)	EV-D68 3A (strain Fermon)	EV-D68 cDNA (strain Fermon)	N-terminus FLAG	pCAGGS
pCAGGS AcGFP-ATF6	ATF6	cDNA from RD cells	N-terminus AcGFP	pCAGGS
pCAGGS FLAG-ATF6	ATF6	cDNA from RD cells	N-terminus FLAG	pCAGGS
pCAGGS AcGFP-GBF1	GBF1	cDNA from RD cells	N-terminus AcGFP	pCAGGS
pCAGGS AcGFP-GBF1 (E794K)	GBF1 (E794K)	pCAGGS AcGFP-GBF1	N-terminus AcGFP	pCAGGS
pCAGGS ARF1-HA	ARF1	cDNA from RD cells	C-terminus HA	pCAGGS
pCAGGS ARF1 (T31N)-HA	ARF1 (T31N)	pCAGGS ARF1-HA	C-terminus HA	pCAGGS
pCAGGS ARF1 (Q71L)-eGFP	ARF1 (Q71L)	pCAGGS ARF1-HA	C-terminus eGFP	pCAGGS
pCAGGS AcGFP-ACBD3	ACBD3	cDNA from RD cells	N-terminus AcGFP	pCAGGS
pCAGGS BiP-HA	BiP	cDNA from RD cells	C-terminus HA	pCAGGS

CTCCT-3′; *CHOP* 5′-GCACCTCCCAGAGCCCTCACTCTCC-3′ and 5′-GTCTACTCCAAGCCTTCCCCCTGCG-3′; *EV-A71* 5′-GCCCCTGAATGCGGCTAAT-3′ and 5′-ATTGTCACCATAAGCAGCCA-3′ and *GBF1* 5′-GGGAACGCATTGACTGTTTT-3′ and 5′-CTCGGGCTTCTCAAAGTCAC-3′; GBF1 5′-GGGAACGCATTGACTGTTTT-3′ and 5′-CTCGGGCTTCTCAAAGTCAC-3′.

siRNA

For the experiment presented in Fig. 9C, silencer select negative control No. 1 siRNA (Cat#4390843) and siGBF1 silencer select pre-designed siRNA (Cat#4427037; ID s16634 and s16635) were obtained from Thermo Fisher Scientific. The siRNAs were transfected into RD cells using Lipofectamine RNAiMAX Transfection Reagent (Thermo Fisher

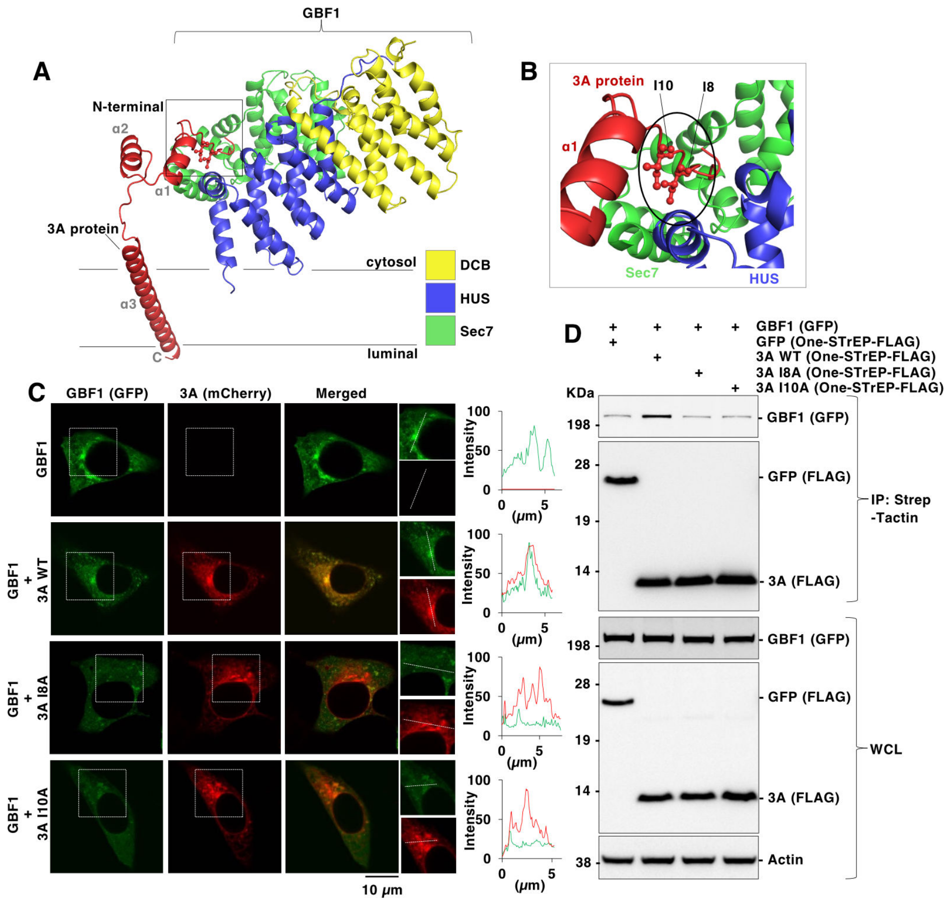

FIG 11 Interaction of Ile^{8} and Ile^{10} of the 3A protein with GBF1. (A) The protein complex of 3A and the N-terminal half of GBF1 was generated using the AlphaFold2 algorithm. The DCB, HUS, and Sec7 domains of GBF1 are indicated in yellow, blue, and green, respectively. (B) A close-up view of the interaction interface of 3A and GBF1. The 3A interacts with GBF1 via amino acid residues I8 and I10. (C) RD cells expressing N-terminal AcGFP-tagged GBF1 and N-terminal mCherry-tagged wild type or mutants of 3A protein and fluorescent signals were detected using microscopy at 48 h post-transfection. The scale bar represents 10 μm. The colocalization analysis was performed using Fiji software (*Right*). (D) HEK293T cells co-expressing GFP-tagged GBF1 with One-STrEP-tagged GFP, One-STrEP-tagged wild type or mutants of 3A protein were subjected to immunoprecipitation assay. Immunoprecipitated samples (IP) and whole-cell lysates (WCL) were subjected to sodium dodecyl sulfate-polyacrylamide gel electrophoresis and immunoblotting. The data presented in C and D are representative of two independent experiments.

Scientific) according to the manufacturer's protocol. The knockdown efficiency was confirmed using immunoblotting and/or qPCR.

Immunoblotting

For preparing lysates, the cells were washed once with phosphate-buffered saline (PBS) and lysed in lysis buffer consisting of 20 mM Tris·HCl (pH 7.4), 135 mM NaCl, 1% Triton X-100, 1% glycerol, and protease inhibitor mixture tablets (Roche). The cell lysates were incubated on ice for 20 min and centrifuged at 15,000 rpm for 5 min at 4°C. The supernatants from the cell lysates were collected and mixed with an equal volume of sodium dodecyl sulfate (SDS) gel-loading buffer (2×) containing 50 mM Tris-HCl (pH = 6.8), 4% SDS, 0.2% bromophenol blue, 10% glycerol, and 200 mM β-mercaptoethanol at 4°C for 1 h. For the experiments presented in Fig. 6B and C, samples were subsequently incubated at 95°C for 5 min. The samples were resolved using SDS polyacrylamide gel electrophoresis (NuPAGE gel, Life Technologies) and transferred onto nitrocellulose membranes (iBlot2, Life Technologies). The membranes were blocked with

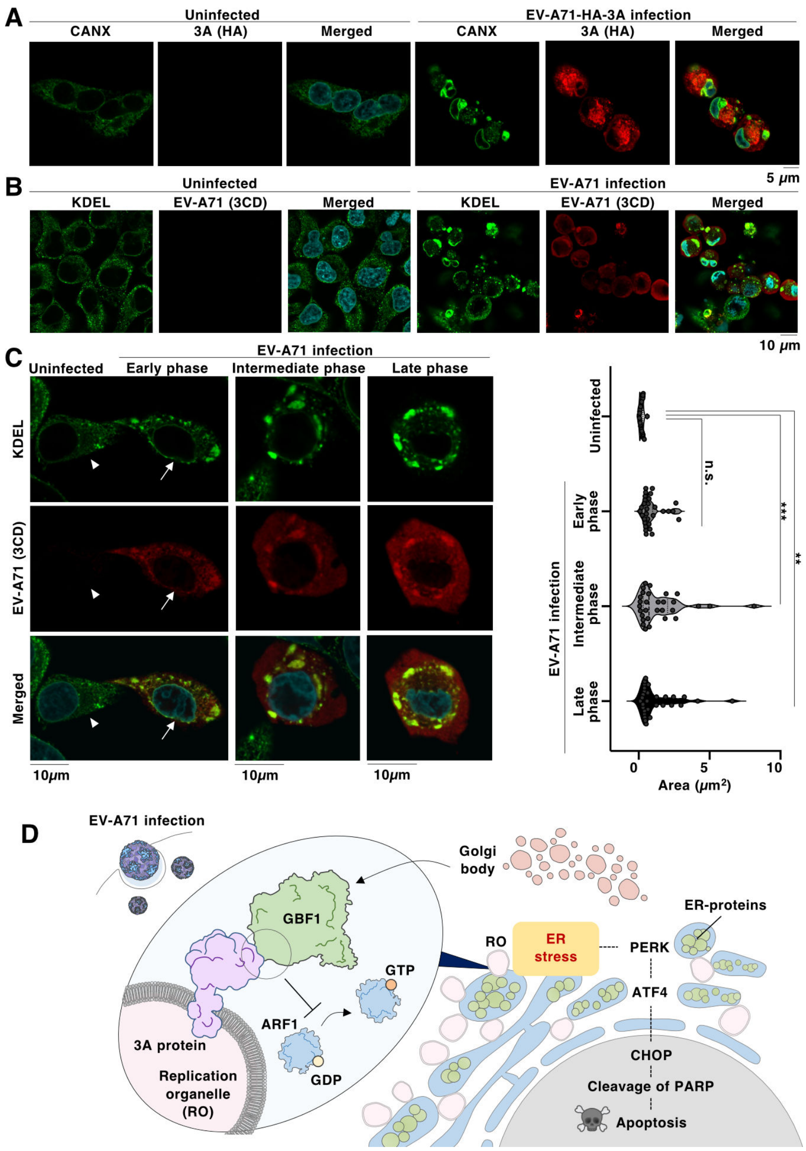

FIG 12 EV-A71 infection induces accumulation of proteins localized in ER. (A) RD cells infected with recombinant EV-A71-HA-3A at an MOI of 0.3 were stained with anti-CANX antibody, anti-HA antibody, and DAPI at 24 h post-infection, and fluorescent signals were detected using microscopy. The scale bar represents 5 µm. (B) RD cells infected with EV-A71 at an MOI of 0.3 were incubated for 30 h and stained with anti-KDEL antibody, anti-EV-A71 3CD antibody, and DAPI. The fluorescent signals were detected using microscopy. The scale bars represent 10 µm. (C) RD cells infected with EV-A71 at an MOI of 0.3 were incubated for 8 h (early phase), 16 h (intermediate phase), or 30 h (late phase) and stained with anti-KDEL antibody, anti-EV-A71 3CD antibody, and DAPI. The fluorescent signals were detected using microscopy. The arrowhead and straight arrow represent uninfected and EV-A71-infected cells, respectively. The scale bars represent 10 µm (*Left*). The cytoplasmic structures of ER-resident proteins were analyzed, and their areas were quantified using Fiji software (n = 30 in each group) (*Right*). (D) Schematic representation of GBF1 hijacking by 3A. Expression of 3A upon infection induces sequestration of GBF1 at RO, inhibiting ARF1 activation. The inhibition of GBF1 affects ER homeostasis, causing activation of the PERK/CHOP-mediated apoptotic branch of UPR. The data presented in A-C are representative of two independent experiments. Significance (**$P \leq 0.01$; ***$P \leq 0.001$; n.s., not significant) was determined using one-way ANOVA test ($n = 30$).

PBS containing 0.05% Tween20 (PBST) supplemented with 5% skim milk for 1 h at room temperature. These membranes were incubated with primary antibodies at 4°C for 24 h, washed thrice with PBST, incubated with secondary antibodies at room temperature for 1 h, and washed thrice with PBST again. The dilutions of primary and secondary antibodies were determined according to the manufacturer's protocol. The blots were developed using the Amersham ECL Western Blotting Detection Reagents (GE Healthcare), and the protein expression was visualized using the LAS-3000 imaging system (FUJIFILM).

Immunoprecipitation

HEK293T cells (2×10^6 cells in 10 mL of culture medium) were seeded on a 10 cm dish and incubated at 37°C for 24 h. The cells were transfected with plasmids using polyethyleneimine (PEI, 1 mg/mL; MW, 25,000) (Polysciences, Inc.) and Opti-MEM (Thermo Fisher Scientific). The cells were harvested at 48 h post-transfection. For the experiment presented in Fig. 8A, cell lysates were incubated with the antibody at 4°C for 24 h and with Protein G Sepharose 4 Fast Flow (Cytiva) at 4°C for 1 h. For the experiment presented in Fig. 11D, cell lysates were incubated with Strep-Taction Sepharose resin (IBA Lifesciences) at 4°C for 24 h. The protein G Sepharose or Strep-Taction beads were washed five times with lysis buffer and incubated with the sample buffer at 60°C for 20 min. The resultant samples were subjected to immunoblotting.

RNA sequencing

ISOGEN II (Nippon Gene) was used to extract total RNAs from RD cells. The sequencing libraries were prepared from the RNAs using a TruSeq stranded mRNA sample prep kit (Illumina, San Diego, CA) according to the manufacturer's protocol. The library was sequenced using an Illumina NovaSeq 6000 platform in a 100 bp single-end mode. The sequenced reads were then mapped to the human reference genome sequences (hg19) using TopHat v2.0.13 in combination with Bowtie2 ver. 2.2.3 and SAMtools ver. 0.1.19. Cufflinks version 2.2.1. was used to calculate the fragments per kilobase of exon per million mapped fragments (FPKMs). GO analysis was performed using iDEP.96 server (http://bioinformatics.sdstate.edu/idep96/) to identify the biological processes (Fig. 8E).

Immunofluorescence staining

Cells (3×10^4 cells in 0.3 mL of culture medium) were seeded on cover glass chambers (IWAKI, 5232-008), incubated at 37°C for 24 h, and subjected to subsequent experiments. Cells fixed with 4% paraformaldehyde in PBS at room temperature for 20 min were washed twice with PBS and permeabilized with 0.2% Triton X-100 in PBS for 20 min. Subsequently, the cells were washed twice with PBS and incubated with primary antibodies at 4°C for 24 h. The concentrations of primary antibodies were determined according to the manufacturer's protocol. The cells were washed twice with PBS, incubated with secondary antibodies (1:1,000 dilution) at room temperature for 1 h, and washed twice with PBS. The cells were then incubated with Cellstain DAPI solution (Dojindo, D523) (1:5,000 dilution) at room temperature for 20 min to visualize the nuclei. The fluorescent signals were observed using microscopy (FV-3000; OLYMPUS) and analyzed using cellSens imaging software (OLYMPUS).

Plaque formation assay

RD cells (1.5×10^5 cells in 0.5 mL of culture medium) seeded on a 24-well plate were incubated at 37°C for 24 h, infected with a serially diluted virus, incubated at 35°C for 1 h, and washed thrice with DMEM supplemented with 2% FBS. After removing the culture supernatants, the infected cells were incubated with DMEM supplemented with cellulose (MERCK, 435244) and 2% FBS. The cellulose in the plaque overlay medium was 0.3% final concentration for EV-A71 and EV-D68, 1.2% for CVB3, or 1% for PV1 and PV3. Cells were incubated with 4% paraformaldehyde (PFA) in PBS for 4 h after incubation at 35°C for 72 h (EV-A71, PV1, and PV3), 48 h (CVB3), and 96 h (EV-D68) and stained with 20% ethanol in PBS containing 0.5% crystal violet.

Caspase activity assay

For the experiments presented in Fig. 6D, RD cells infected with EV-A71 at an MOI of 0.3 were incubated with PERKi I at a concentration of 3 µM for 24 h. For the experiments presented in Fig. 6F, RD cells were transfected with an increased concentration of 3A plasmid and incubated for 48 h. Caspase activity was determined using the Caspase-Glo 3/7 Assay System (G8091; Promega) according to the manufacturer's protocol.

Structural modeling of the 3A protein and GBF1

For the experiment presented in Fig. 7K, a structural model of the N-terminal domain of the 3A protein was developed using the I-TASSER (Iterative Threading ASSEmbly Refinement) server (https://zhanggroup.org/I-TASSER/). For the experiment presented in Fig. 11A and B, the complex structure of the 3A protein and GBF1 was predicted using AlphaFold2_advanced (https://colab.research.google.com/github/sokrypton/ColabFold/blob/main/beta/AlphaFold2_advanced.ipynb). The electric potential was calculated using an Adaptive Poisson–Boltzmann Solver (APBS) tool. The structure images were obtained using PyMOL (the open-source PyMOL Molecular Graphics System 1.8.4.0).

Statistical analysis

For the experiments presented in Fig. 1F, 10H, and 11C, the colocalization analysis and the image area calculations were performed using Fiji software (ImageJ2 Version: 2.3.0/1.53 f). All statistical analyses were performed using GraphPad Prism version 9.5.1 (GraphPad). The significant differences were determined using the ANOVA test or the Student's *t*-test, and the statistical analysis employed in each experiment is described in the figure legends.

ACKNOWLEDGMENTS

We thank M. Tomiyama, T. Toyoshima, A. Tanaka, M. Ishibashi, and K. Toyoda for their assistance. We want to thank all members of the Department of Virology II, National Institute of Infectious Diseases, for their kind support and advice. We acknowledge the NGS core facility of the Genome Information Research Center at the Research Institute for Microbial Diseases of Osaka University for its support in RNA sequencing and data analysis.

This work was partly supported by the Ministry of Education, Culture, Sports, Science, and Technology of Japan (KAKENHI) (grant numbers JP22K15479 and JP22K06625), the Japan Agency for Medical Research and Development (AMED) (grant number JP22fk0108627j0601), the SENSHIN Medical Research Foundation, and Japan Science and Technology Agency (JST) (Moonshot R&D) (JPMJMS2025). This research was conducted as part of the All-Osaka U Research in "The Nippon Foundation - Osaka University Project for Infectious Disease Prevention".

AUTHOR AFFILIATIONS

[1]Laboratory of Virus Control, Center for Infectious Disease Education and Research (CiDER), Osaka, Japan
[2]Research Institute for Microbial Diseases (RIMD), Osaka University, Osaka, Japan
[3]Department of Virology II, National Institute of Infectious Diseases, Tokyo, Japan
[4]Institute for Advanced Co-Creation Studies, Research Institute for Microbial Diseases, Osaka University, Osaka, Japan
[5]Department of Microbiology, Juntendo University School of Medicine, Tokyo, Japan

[6]Center for Advanced Modalities and DDS (CAMaD), Osaka University, Osaka, Japan
[7]Department of Infectious Disease Research, Institute of Biomedical Research and Innovation, Foundation for Biomedical Research and Innovation at Kobe, Kobe, Japan

AUTHOR ORCIDs

Junki Hirano http://orcid.org/0009-0003-9254-8937
Kouichi Kitamura http://orcid.org/0000-0001-9692-8724
Kazuma Okada http://orcid.org/0000-0002-7775-5984
Yoshiharu Matsuura http://orcid.org/0000-0001-9091-8285

FUNDING

Funder	Grant(s)	Author(s)
Ministry of Education, Culture, Sports, Science and Technology (MEXT)	JP22K15479	Junki Hirano
Ministry of Education, Culture, Sports, Science and Technology (MEXT)	JP22K06625	Junki Hirano
Japan Agency for Medical Research and Development (AMED)	JP22fk0108627j0601	Junki Hirano
SENSHIN Medical Research Foundation (SMRF)		Junki Hirano
MEXT | Japan Science and Technology Agency (JST)	JPMJMS2025	Yoshiharu Matsuura

DATA AVAILABILITY

RNA-seq data have been deposited into the NCBI Gene Expression Omnibus Repository (Accession No. GSE268418). All data are presented in the main figures. Raw sequencing data and microscopy images, materials, and sequence information are available upon request. Correspondence and requests for materials should be addressed to Professor Yoshiharu Matsuura.

REFERENCES

1. Baumann O, Walz B. 2001. Endoplasmic reticulum of animal cells and its organization into structural and functional domains. Int Rev Cytol 205:149–214. https://doi.org/10.1016/s0074-7696(01)05004-5
2. Reimertz C, Kögel D, Rami A, Chittenden T, Prehn JHM. 2003. Gene expression during ER stress-induced apoptosis in neurons: induction of the BH3-only protein Bbc3/PUMA and activation of the mitochondrial apoptosis pathway. J Cell Biol 162:587–597. https://doi.org/10.1083/jcb.200305149
3. Wang M, Kaufman RJ. 2016. Protein misfolding in the endoplasmic reticulum as a conduit to human disease. Nature 529:326–335. https://doi.org/10.1038/nature17041
4. Choi JA, Song CH. 2019. Insights into the role of endoplasmic reticulum stress in infectious diseases. Front Immunol 10:3147. https://doi.org/10.3389/fimmu.2019.03147
5. Li S, Kong L, Yu X. 2015. The expanding roles of endoplasmic reticulum stress in virus replication and pathogenesis. Crit Rev Microbiol 41:150–164. https://doi.org/10.3109/1040841X.2013.813899
6. Lugo D, Krogstad P. 2016. Enteroviruses in the early 21st century: new manifestations and challenges. Curr Opin Pediatr 28:107–113. https://doi.org/10.1097/MOP.0000000000000303
7. Huang SW, Cheng D, Wang JR. 2019. Enterovirus A71: virulence, antigenicity, and genetic evolution over the years. J Biomed Sci 26:81. https://doi.org/10.1186/s12929-019-0574-1
8. Baggen J, Thibaut HJ, Strating JRPM, van Kuppeveld FJM. 2018. The life cycle of non-polio enteroviruses and how to target it. Nat Rev Microbiol 16:368–381. https://doi.org/10.1038/s41579-018-0005-4
9. Suhy DA, Giddings TH, Kirkegaard K. 2000. Remodeling the endoplasmic reticulum by poliovirus infection and by individual viral proteins: an autophagy-like origin for virus-induced vesicles. J Virol 74:8953–8965. https://doi.org/10.1128/jvi.74.19.8953-8965.2000
10. Wessels E, Duijsings D, Lanke KHW, Melchers WJG, Jackson CL, van Kuppeveld FJM. 2007. Molecular determinants of the interaction between coxsackievirus protein 3A and guanine nucleotide exchange factor GBF1. J Virol 81:5238–5245. https://doi.org/10.1128/JVI.02680-06
11. Greninger AL, Knudsen GM, Betegon M, Burlingame AL, Derisi JL. 2012. The 3A protein from multiple picornaviruses utilizes the golgi adaptor protein ACBD3 to recruit PI4KIIIβ. J Virol 86:3605–3616. https://doi.org/10.1128/JVI.06778-11
12. Horova V, Lyoo H, Różycki B, Chalupska D, Smola M, Humpolickova J, Strating JRPM, van Kuppeveld FJM, Boura E, Klima M. 2019. Convergent evolution in the mechanisms of ACBD3 recruitment to picornavirus replication sites. PLoS Pathog 15:e1007962. https://doi.org/10.1371/journal.ppat.1007962
13. Rattanakomol P, Srimanote P, Tongtawe P, Khantisitthiporn O, Supasorn O, Thanongsaksrikul J. 2022. Host neuronal PRSS3 interacts with enterovirus A71 3A protein and its role in viral replication. Sci Rep 12:12846. https://doi.org/10.1038/s41598-022-17272-2
14. Lu JY, Brewer G, Li ML, Lin KZ, Huang CC, Yen LC, Lin JY. 2021. Secretory carrier membrane protein 3 interacts with 3A viral protein of enterovirus and participates in viral replication. Microbiol Spectr 9:e0047521.
15. Doedens JR, Kirkegaard K. 1995. Inhibition of cellular protein secretion by poliovirus proteins 2B and 3A. EMBO J 14:894–907. https://doi.org/10.1002/j.1460-2075.1995.tb07071.x

16. Wessels E, Duijsings D, Notebaart RA, Melchers WJG, van Kuppeveld FJM. 2005. A proline-rich region in the coxsackievirus 3a protein is required for the protein to inhibit endoplasmic reticulum-to-golgi transport. J Virol 79:5163–5173. https://doi.org/10.1128/JVI.79.8.5163-5173.2005
17. Welsch S, Miller S, Romero-Brey I, Merz A, Bleck CKE, Walther P, Fuller SD, Antony C, Krijnse-Locker J, Bartenschlager R. 2009. Composition and three-dimensional architecture of the dengue virus replication and assembly sites. Cell Host Microbe 5:365–375. https://doi.org/10.1016/j.chom.2009.03.007
18. Cortese M, Goellner S, Acosta EG, Neufeldt CJ, Oleksiuk O, Lampe M, Haselmann U, Funaya C, Schieber N, Ronchi P, Schorb M, Pruunsild P, Schwab Y, Chatel-Chaix L, Ruggieri A, Bartenschlager R. 2017. Ultrastructural characterization of zika virus replication factories. Cell Rep 18:2113–2123. https://doi.org/10.1016/j.celrep.2017.02.014
19. Romero-Brey I, Merz A, Chiramel A, Lee JY, Chlanda P, Haselman U, Santarella-Mellwig R, Habermann A, Hoppe S, Kallis S, Walther P, Antony C, Krijnse-Locker J, Bartenschlager R. 2012. Three-dimensional architecture and biogenesis of membrane structures associated with hepatitis C virus replication. PLoS Pathog 8:e1003056. https://doi.org/10.1371/journal.ppat.1003056
20. Wolff G, Melia CE, Snijder EJ, Bárcena M. 2020. Double-membrane vesicles as platforms for viral replication. Trends Microbiol 28:1022–1033. https://doi.org/10.1016/j.tim.2020.05.009
21. Wang Q, Xin X, Wang T, Wan J, Ou Y, Yang Z, Yu Q, Zhu L, Guo Y, Wu Y, Ding Z, Zhang Y, Pan Z, Tang Y, Li S, Kong L. 2019. Japanese encephalitis virus induces apoptosis and encephalitis by activating the PERK pathway. J Virol 93:e00887-19. https://doi.org/10.1128/JVI.00887-19
22. Chan CP, Siu KL, Chin KT, Yuen KY, Zheng B, Jin DY. 2006. Modulation of the unfolded protein response by the severe acute respiratory syndrome coronavirus spike protein. J Virol 80:9279–9287. https://doi.org/10.1128/JVI.00659-06
23. Chu H, Shuai H, Hou Y, Zhang X, Wen L, Huang X, Hu B, Yang D, Wang Y, Yoon C, Wong BH-Y, Li C, Zhao X, Poon VK-M, Cai J-P, Wong KK-Y, Yeung M-L, Zhou J, Au-Yeung RK-H, Yuan S, Jin D-Y, Kok K-H, Perlman S, Chan JF-W, Yuen K-Y. 2021. Targeting highly pathogenic coronavirus-induced apoptosis reduces viral pathogenesis and disease severity. Sci Adv 7. https://doi.org/10.1126/sciadv.abf8577
24. Melia CE, Peddie CJ, de Jong AWM, Snijder EJ, Collinson LM, Koster AJ, van der Schaar HM, van Kuppeveld FJM, Bárcena M. 2019. Origins of enterovirus replication organelles established by whole-cell electron microscopy. mBio 10:e00951-19. https://doi.org/10.1128/mBio.00951-19
25. Laufman O, Perrino J, Andino R. 2019. Viral generated inter-organelle contacts redirect lipid flux for genome replication. Cell 178:275–289. https://doi.org/10.1016/j.cell.2019.05.030
26. Sarnow P. 1989. Translation of glucose-regulated protein 78/immunoglobulin heavy-chain binding protein mRNA is increased in poliovirus-infected cells at a time when cap-dependent translation of cellular mRNAs is inhibited. Proc Natl Acad Sci U S A 86:5795–5799. https://doi.org/10.1073/pnas.86.15.5795
27. Yang Q, Sarnow P. 1997. Location of the internal ribosome entry site in the 5' non-coding region of the immunoglobulin heavy-chain binding protein (BiP) mRNA: evidence for specific RNA-protein interactions. Nucleic Acids Res 25:2800–2807. https://doi.org/10.1093/nar/25.14.2800
28. Jheng J-R, Lau KS, Tang W-F, Wu M, Horng J-T. 2010. Endoplasmic reticulum stress is induced and modulated by enterovirus 71. Cell Microbiol 12:796–813. https://doi.org/10.1111/j.1462-5822.2010.01434.x
29. Ge M, Luo Z, Qiao Z, Zhou Y, Cheng X, Geng Q, Cai Y, Wan P, Xiong Y, Liu F, Wu K, Liu Y, Wu J. 2017. HERP binds TBK1 to activate innate immunity and repress virus replication in response to endoplasmic reticulum stress. J Immunol 199:3280–3292. https://doi.org/10.4049/jimmunol.1700376
30. Zhang HM, Ye X, Su Y, Yuan J, Liu Z, Stein DA, Yang D. 2010. Coxsackievirus B3 infection activates the unfolded protein response and induces apoptosis through downregulation of p58IPK and activation of CHOP and SREBP1. J Virol 84:8446–8459. https://doi.org/10.1128/JVI.01416-09
31. Smee DF, Evans WJ, Nicolaou KC, Tarbet EB, Day CW. 2016. Susceptibilities of enterovirus D68, enterovirus 71, and rhinovirus 87 strains to various antiviral compounds. Antiviral Res 131:61–65. https://doi.org/10.1016/j.antiviral.2016.04.003
32. Zhang X, Song Z, Qin B, Zhang X, Chen L, Hu Y, Yuan Z. 2013. Rupintrivir is a promising candidate for treating severe cases of enterovirus-71 infection: evaluation of antiviral efficacy in a murine infection model. Antiviral Res 97:264–269. https://doi.org/10.1016/j.antiviral.2012.12.029
33. Doedens JR, Giddings TH, Kirkegaard K. 1997. Inhibition of endoplasmic reticulum-to-golgi traffic by poliovirus protein 3A: genetic and ultrastructural analysis. J Virol 71:9054–9064. https://doi.org/10.1128/JVI.71.12.9054-9064.1997
34. Moon JL, Kim SY, Shin SW, Park JW. 2012. Regulation of brefeldin A-induced ER stress and apoptosis by mitochondrial NADP$^+$-dependent Isocitrate dehydrogenase. Biochem Biophys Res Commun 417:760–764. https://doi.org/10.1016/j.bbrc.2011.12.030
35. Claude A, Zhao BP, Kuziemsky CE, Dahan S, Berger SJ, Yan JP, Armold AD, Sullivan EM, Melançon P. 1999. GBF1: a novel golgi-associated BFA-resistant guanine nucleotide exchange factor that displays specificity for ADP-ribosylation factor 5. J Cell Biol 146:71–84.
36. Saraste J, Dale HA, Bazzocco S, Marie M. 2009. Emerging new roles of the pre-golgi intermediate compartment in biosynthetic-secretory trafficking. FEBS Letters 583:3804–3810. https://doi.org/10.1016/j.febslet.2009.10.084
37. Niu TK, Pfeifer AC, Lippincott-Schwartz J, Jackson CL. 2005. Dynamics of GBF1, a brefeldin A-sensitive Arf1 exchange factor at the golgi. Mol Biol Cell 16:1213–1222. https://doi.org/10.1091/mbc.e04-07-0599
38. Greninger AL. 2015. Picornavirus--host interactions to construct viral secretory membranes. Prog Mol Biol Transl Sci 129:189–212. https://doi.org/10.1016/bs.pmbts.2014.10.007
39. Citterio C, Vichi A, Pacheco-Rodriguez G, Aponte AM, Moss J, Vaughan M. 2008. Unfolded protein response and cell death after depletion of brefeldin A-inhibited guanine nucleotide-exchange protein GBF1. Proc Natl Acad Sci USA 105:2877–2882. https://doi.org/10.1073/pnas.0712224105
40. Lopes-da-Silva M, McCormack JJ, Burden JJ, Harrison-Lavoie KJ, Ferraro F, Cutler DF. 2019. A GBF1-dependent mechanism for environmentally responsive regulation of ER-golgi transport. Dev Cell 49:786–801. https://doi.org/10.1016/j.devcel.2019.04.006
41. García-Mata R, Szul T, Alvarez C, Sztul E. 2003. ADP-ribosylation factor/COPI-dependent events at the endoplasmic reticulum-golgi interface are regulated by the guanine nucleotide exchange factor GBF1. Mol Biol Cell 14:2250–2261. https://doi.org/10.1091/mbc.e02-11-0730
42. Dascher C, Balch WE. 1994. Dominant inhibitory mutants of Arf1 block endoplasmic reticulum to golgi transport and trigger disassembly of the golgi apparatus. J Biol Chem 269:1437–1448.
43. Hsu N-Y, Ilnytska O, Belov G, Santiana M, Chen Y-H, Takvorian PM, Pau C, van der Schaar H, Kaushik-Basu N, Balla T, Cameron CE, Ehrenfeld E, van Kuppeveld FJM, Altan-Bonnet N. 2010. Viral reorganization of the secretory pathway generates distinct organelles for RNA replication. Cell 141:799–811. https://doi.org/10.1016/j.cell.2010.03.050
44. Wessels E, Duijsings D, Niu T-K, Neumann S, Oorschot VM, de Lange F, Lanke KHW, Klumperman J, Henke A, Jackson CL, Melchers WJG, van Kuppeveld FJM. 2006. A viral protein that blocks Arf1-mediated COP-I assembly by inhibiting the guanine nucleotide exchange factor GBF1. Dev Cell 11:191–201. https://doi.org/10.1016/j.devcel.2006.06.005
45. Lin JH, Walter P, Yen TSB. 2008. Endoplasmic reticulum stress in disease pathogenesis. Annu Rev Pathol 3:399–425. https://doi.org/10.1146/annurev.pathmechdis.3.121806.151434
46. Ogen-Shtern N, Chang C, Saad H, Mazkereth N, Patel C, Shenkman M, Lederkremer GZ. 2023. COP I and II dependent trafficking controls ER-associated degradation in mammalian cells. iScience 26:106232. https://doi.org/10.1016/j.isci.2023.106232
47. Kokubun H, Jin H, Aoe T. 2019. Pathogenic effects of impaired retrieval between the endoplasmic reticulum and golgi complex. Int J Mol Sci 20:5614. https://doi.org/10.3390/ijms20225614
48. Lanke KHW, van der Schaar HM, Belov GA, Feng Q, Duijsings D, Jackson CL, Ehrenfeld E, van Kuppeveld FJM. 2009. GBF1, a guanine nucleotide exchange factor for arf, is crucial for coxsackievirus B3 RNA replication. J Virol 83:11940–11949. https://doi.org/10.1128/JVI.01244-09
49. Deitz SB, Dodd DA, Cooper S, Parham P, Kirkegaard K. 2000. MHC I-dependent antigen presentation is inhibited by poliovirus protein 3A. Proc Natl Acad Sci U S A 97:13790–13795. https://doi.org/10.1073/pnas.250483097
50. Neznanov N, Kondratova A, Chumakov KM, Angres B, Zhumabayeva B, Agol VI, Gudkov AV. 2001. Poliovirus protein 3A inhibits tumor necrosis factor (TNF)-Induced apoptosis by eliminating the TNF receptor from the

cell surface. J Virol 75:10409–10420. https://doi.org/10.1128/JVI.75.21.10409-10420.2001
51. Gazina EV, Mackenzie JM, Gorrell RJ, Anderson DA. 2002. Differential requirements for COPI coats in formation of replication complexes among three genera of picornaviridae. J Virol 76:11113–11122. https://doi.org/10.1128/jvi.76.21.11113-11122.2002
52. O'Donnell VK, Pacheco JM, Henry TM, Mason PW. 2001. Subcellular distribution of the foot-and-mouth disease virus 3A protein in cells infected with viruses encoding wild-type and bovine-attenuated forms of 3A. Virology 287:151–162. https://doi.org/10.1006/viro.2001.1035
53. Irurzun A, Perez L, Carrasco L. 1992. Involvement of membrane traffic in the replication of poliovirus genomes: effects of brefeldin A. Virology 191:166–175. https://doi.org/10.1016/0042-6822(92)90178-r
54. Sasaki J, Ishikawa K, Arita M, Taniguchi K. 2012. ACBD3-mediated recruitment of PI4KB to picornavirus RNA replication sites. EMBO J 31:754–766. https://doi.org/10.1038/emboj.2011.429
55. Ranjitha HB, Ammanathan V, Guleria N, Hosamani M, Sreenivasa BP, Dhanesh VV, Santhoshkumar R, Sagar BKC, Mishra BP, Singh RK, Sanyal A, Manjithaya R, Basagoudanavar SH. 2020. Foot-and-mouth disease virus induces PERK-mediated autophagy to suppress the antiviral interferon response. J Cell Sci 134. https://doi.org/10.1242/jcs.240622
56. Hou L, Ge X, Xin L, Zhou L, Guo X, Yang H. 2014. Nonstructural proteins 2C and 3d are involved in autophagy as induced by the encephalomyocarditis virus. Virol J 11:156. https://doi.org/10.1186/1743-422X-11-156
57. Wang J, Du J, Jin Q. 2014. Class I ADP-ribosylation factors are involved in enterovirus 71 replication. PLoS One 9:e99768. https://doi.org/10.1371/journal.pone.0099768
58. Wessels E, Notebaart RA, Duijsings D, Lanke K, Vergeer B, Melchers WJG, van Kuppeveld FJM. 2006. Structure-function analysis of the coxsackievirus protein 3A: identification of residues important for dimerization, viral RNA replication, and transport inhibition. J Biol Chem 281:28232–28243. https://doi.org/10.1074/jbc.M601122200
59. Li M-L, Lin J-Y, Chen B-S, Weng K-F, Shih S-R, Calderon JD, Tolbert BS, Brewer G. 2019. EV71 3C protease induces apoptosis by cleavage of hnRNP A1 to promote apaf-1 translation. PLoS One 14:e0221048. https://doi.org/10.1371/journal.pone.0221048
60. Goldstaub D, Gradi A, Bercovitch Z, Grosmann Z, Nophar Y, Luria S, Sonenberg N, Kahana C. 2000. Poliovirus 2a protease induces apoptotic cell death. Mol Cell Biol 20:1271–1277. https://doi.org/10.1128/MCB.20.4.1271-1277.2000
61. Barco A, Feduchi E, Carrasco L. 2000. Poliovirus protease 3C(pro) kills cells by apoptosis. Virology 266:352–360. https://doi.org/10.1006/viro.1999.0043
62. Suzuki T, Okamoto T, Katoh H, Sugiyama Y, Kusakabe S, Tokunaga M, Hirano J, Miyata Y, Fukuhara T, Ikawa M, Satoh T, Yoshio S, Suzuki R, Saijo M, Huang DCS, Kanto T, Akira S, Matsuura Y. 2018. Infection with flaviviruses requires BCLXL for cell survival. PLoS Pathog 14:e1007299. https://doi.org/10.1371/journal.ppat.1007299
63. Tan CW, Tee HK, Lee MHP, Sam I-C, Chan YF. 2016. Enterovirus A71 DNA-launched infectious clone as a robust reverse genetic tool. PLoS One 11:e0162771. https://doi.org/10.1371/journal.pone.0162771
64. Shimizu H, Utama A, Yoshii K, Yoshida H, Yoneyama T, Sinniah M, Yusof MA, Okuno Y, Okabe N, Shih SR, Chen HY, Wang GR, Kao CL, Chang KS, Miyamura T, Hagiwara A. 1999. Enterovirus 71 from fatal and nonfatal cases of hand, foot and mouth disease epidemics in Malaysia, Japan and Taiwan in 1997-1998. Jpn J Infect Dis 52:12–15.
65. Lopacinski AB, Sweatt AJ, Smolko CM, Gray-Gaillard E, Borgman CA, Shah M, Janes KA. 2021. Modeling the complete kinetics of coxsackievirus B3 reveals human determinants of host-cell feedback. Cell Syst 12:304–323. https://doi.org/10.1016/j.cels.2021.02.004
66. Pan J, Narayanan B, Shah S, Yoder JD, Cifuente JO, Hafenstein S, Bergelson JM. 2011. Single amino acid changes in the virus capsid permit coxsackievirus B3 to bind decay-accelerating factor. J Virol 85:7436–7443. https://doi.org/10.1128/JVI.00503-11
67. van der Schaar HM, Melia CE, van Bruggen JAC, Strating J, van Geenen MED, Koster AJ, Bárcena M, van Kuppeveld FJM. 2016. Illuminating the sites of enterovirus replication in living cells by using a split-GFP-tagged viral protein. mSphere 1:e00104-16. https://doi.org/10.1128/mSphere.00104-16